Apparent Diffusion Coefficients from High Angular Resolution Diffusion Images: Estimation and Applications

Maxime Descoteaux, Elaine Angelino, Shaun Fitzgibbons, Rachid Deriche

▶ **To cite this version:**

Maxime Descoteaux, Elaine Angelino, Shaun Fitzgibbons, Rachid Deriche. Apparent Diffusion Coefficients from High Angular Resolution Diffusion Images: Estimation and Applications. [Research Report] RR-5681, INRIA. 2006, pp.44. inria-00070332

HAL Id: inria-00070332
https://inria.hal.science/inria-00070332

Submitted on 19 May 2006

HAL is a multi-disciplinary open access archive for the deposit and dissemination of scientific research documents, whether they are published or not. The documents may come from teaching and research institutions in France or abroad, or from public or private research centers.

L'archive ouverte pluridisciplinaire **HAL**, est destinée au dépôt et à la diffusion de documents scientifiques de niveau recherche, publiés ou non, émanant des établissements d'enseignement et de recherche français ou étrangers, des laboratoires publics ou privés.

INRIA

INSTITUT NATIONAL DE RECHERCHE EN INFORMATIQUE ET EN AUTOMATIQUE

Apparent Diffusion Coefficients from High Angular Resolution Diffusion Images: Estimation and Applications

Maxime Descoteaux — Elaine Angelino — Shaun Fitzgibbons — Rachid Deriche

N° 5681

Septembre 2005

Thème BIO

ISSN 0249-6399 ISRN INRIA/RR--5681--FR+ENG

Apparent Diffusion Coefficients from High Angular Resolution Diffusion Images: Estimation and Applications

Maxime Descoteaux* , Elaine Angelino† , Shaun Fitzgibbons‡ , Rachid Deriche§

Thème BIO —Systèmes biologiques
Projet Odyssée

Rapport de recherche n° 5681 —Septembre 2005 — 44 pages

Abstract: High angular resolution diffusion imaging (HARDI) has recently been of great interest in characterizing non-Gaussian diffusion processes. In the white matter of the brain, non-Gaussian diffusion occurs when fiber bundles cross, kiss or diverge within the same voxel. One important goal in current research is to obtain more accurate fits of the apparent diffusion processes in these multiple fiber regions, thus overcoming the limitations of classical diffusion tensor imaging (DTI). This paper presents an extensive study of high order models for apparent diffusion coefficient estimation and illustrates some of their applications. In particular, we first develop the appropriate mathematical tools to work on noisy HARDI data. Using a meaningful modified spherical harmonics basis to capture the physical constraints of the problem, we propose a new regularization algorithm to estimate a diffusivity profile smoother and closer to the true diffusivities without noise. We define a smoothing term based on the Laplace-Beltrami operator for functions defined on the unit sphere. The properties of the spherical harmonics are then exploited to derive a closed form implementation of this term into the fitting procedure. We next derive the general linear transformation between the coefficients of a spherical harmonics series of order ℓ and the independent elements of the rank-ℓ high order diffusion tensor. An additional contribution of the paper is the careful study of the state of the art anisotropy measures for high order formulation models computed from spherical harmonics or tensor coefficients. Their ability to characterize the underlying diffusion process is analyzed. We are able to reproduce published results and also able to recover voxels with isotropic, single fiber anisotropic and multiple fiber anisotropic diffusion. We test and validate the different approaches on apparent diffusion coefficients from synthetic data, from a biological phantom and from a human brain dataset.

Key-words: restoration and deblurring, high angular resolution diffusion imaging (HARDI), apparent diffusion coefficient (ADC), spherical harmonics (SH), diffusion tensor, anisotropy measure

* Maxime.Descoteaux@sophia.inria.fr
† angelino@fas.harvard.edu
‡ fi tzgibb@fas.harvard.edu
§ Rachid.Deriche@sophia.inria.fr

Coefficients de Diffusion Apparents à Partir d'IRM de Diffusion à Haute Résolution Angulaire: Estimation et Applications

Résumé : L'IRM de diffusion à haute résolution angulaire (HARDI) est maintenant un outil essentiel pour décrire les phénomènes de diffusion non-Gaussiens des faisceaux de fibres de la matière blanche. Ceux-ci se produient lorsque plusieurs fibres se croisent. Dans ce cas, le tenseur de diffusion classique (DTI) est limité et insuffisant. Ce rapport fait le point sur les techniques d'approximations des coefficients de diffusion apparents à partir de modèles à ordres supérieurs et présente aussi leur application dans la définition de mesures d'anisotropies. En particulier, nous développons les outils mathématiques adéquats pour traiter et estimer les coefficients de diffusion bruités provenant des données HARDI. À partir d'une base modifiée d'harmoniques sphériques et de ses propriétés, nous proposons une nouvelle méthode de régularization obtenant des coefficients de diffusion plus lisses. Nous validons l'approche sur des données synthétiques, sur un fantôme biologique et sur un cerveau humain. De plus, nous étudions l'état de l'art des mesures d'anisotropies calculées à partir de modèles à ordres supérieurs et nous évaluons leur habilité à décrire le processus de diffusion.

Mots-clés : restoration et débruitage, IRM de diffusion à haute résolution angulaire (HARDI), coefficient de diffusion apparent (ADC), harmoniques sphériques, tenseur de diffusion, mesure d'anisotropie

Contents

1 Introduction **4**

2 High Angular Resolution Diffusion Imaging (HARDI) **5**

3 Apparent Diffusion Coefficient (ADC) Profile Estimation **7**
3.1 Estimating the ADC Profile with the Spherical Harmonics (SH) 7
3.1.1 Spherical Harmonics (SH) 7
3.1.2 Methods for Fitting Spherical Data with SH Series 8
3.2 Fitting the ADC Profile with a High Order Diffusion Tensor (HODT) 10

4 Fitting HODTs to HARDI Data Using Spherical Harmonics **12**
4.1 A Regularization Algorithm for ADC Profile Estimation 12
4.2 From SH Coefficients to HODT Coefficients 15

5 Synthetic Data Experiments **19**
5.1 Quantitative Comparison 20
5.1.1 Effect of the λ-Regularization Weight 21
5.2 Anisotropy Measures 25
5.2.1 Frank and Chen et al Measures 25
5.2.2 Alexander et al Measure 25
5.2.3 Results of Anisotropy Measures from SH Series 26
5.2.4 Generalized Anisotropy Measure 27
5.2.5 Cumulative Residual Entropy (CRE) 31

6 Real Data Experiment **33**
6.1 A Biological Phantom 33
6.2 Human Brain HARDI Data 33

7 Conclusion and Discussion **38**

A Relation of Spherical Harmonics to the HODT **43**

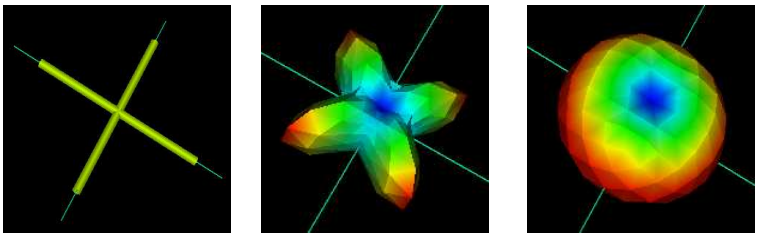

2 fibers true ADC profile ADC profile from DTI

Figure 1: ADC profile estimate from DTI fails to recover multiple fiber orientation. The maxima of the ADC profile do not agree with thin green lines corresponding to the true synthetic fiber directions.

1 Introduction

For the past decade, there has been a growing interest in diffusion magnetic resonance imaging (MRI) to understand functional coupling between cortical regions of the brain, for characterization of neuro-degenerative diseases, for surgical planning and for other medical applications. Diffusion MRI is the only non-invasive tool to obtain information about the neural architecture in vivo. It is based on the Brownian motion of water molecules in normal tissues and the observation that molecules tend to diffuse along fibers when contained in fiber bundles [19, 4]. Using classical diffusion tensor imaging (DTI), several methods have been developed to segment and track white matter fibers in the human brain [39, 45, 47, 8, 23, 24]. The common way to analyze the data is to fit it to a second order tensor, which corresponds to the probability distribution of a given water molecule moving by a certain amount during some fixed elapsed time. By diagonalization, the surface corresponding to the diffusion tensor is an ellipsoid with its long axis aligned with the fiber orientation. However, the theoretical basis for this model assumes that the underlying diffusion process is Gaussian. While this approximation is adequate for voxels in which there is only a single fiber orientation (or none), it breaks down for voxels in which there is more complicated internal structure, as seen in Fig. 1, an example of two fibers crossing. This is an important limitation, since resolution of DTI acquisition is between 1mm^3 and 3mm^3 while the physical diameter of fibers can be less than 1μm and up to 30 μm [30]. From anisotropy measure maps, we know that many voxels in diffusion MRI volumes potentially have multiple fibers with crossing, kissing or diverging configurations.

To date, this is a reason why clinicians and neurosurgeons have been skeptical of tracking and segmentation methods developed on DTI data. They have doubts on the principal directions extracted and followed from the diffusion tensor to track fiber bundles. In the presence of multiple fibers, the diffusion profile is oblate or planar and there is no unique principal direction (Fig. 1). Additionally, note that maxima of the apparent diffusion coefficient (ADC) profile do not correspond to true fiber orientation (thin green lines). In current clinical applications, people instead choose to use simple anisotropy maps computed from the ADC profile [13] to infer white matter connectivity information. These measures are fast and easy to interpret with regions of anisotropy that clearly stand out. Many anisotropy measures exist and the most commonly used are FA (fractional

anisotropy) and RA (relative anisotropy) [5] but again, these measures are limited in non-Gaussian diffusion areas when computed from DTI data. This is well illustrated in Ozarslan et al [29] where the anisotropy measure in a fiber crossing region is in the same range as voxels with no structure. As such, recent research has been done to generalize the existing diffusion model with new higher resolution acquisition techniques such as high angular resolution diffusion imaging (HARDI) [40]. One natural generalization is to model the apparent diffusion coefficient (ADC) with higher order diffusion tensors (HODT) [28]. This model does not assume any a priori knowledge about the diffusivity profile and has the potential to describe non-Gaussian diffusion.

In this article, we study the estimate of the ADC profile from HARDI data and its ability to describe complex tissue architecture. Contrary to most recent papers on HARDI data processing, we do not focus on finding the orientation of underlying fibers but want to design the appropriate tools to describe noisy HARDI data and explore scalar anisotropy measures computed from high order formulation. In particular, the paper addresses the problem of fitting HARDI data with a higher order tensor. One proposed possibility by Ozarslan et al [28] is to use a direct linear regression by least-squares fitting. This can be effective but its robustness to noise is questionable as there does not appear to be any straightforward way to impose a viable smoothness maximizing criteria. We approach the problem with a spherical harmonics series approximation [15, 2, 10]. An important contribution of our work is to propose a generalization of the standard least-squares evaluation method to include a regularization criterion. From this result, we compute the linear transformation taking the coefficients of the spherical harmonic series to the independent elements of the HODT using the relation presented in [28]. Therefore, our approach as well as any technique developed for spherical harmonic formulation can be quickly and easily applied to the high order diffusion tensor formulation and vice versa. This bridge is very useful for comparison purposes between state of the art anisotropy measures for high order models computed from spherical harmonics and tensor coefficients. Published results are reproduced accurately and it is also possible to recover voxels with isotropic, single fiber anisotropic and multiple fiber anisotropic diffusion.

The paper is outlined as follows. In Section 2, we review the basic principle of diffusion MRI and the differences between DTI and HARDI data. In Section 3, we review the existing state of the art techniques to estimate the ADC profile from noisy HARDI data. In Section 4, we propose a new regularization method which recovers a smoother ADC that is closer to the ADC without noise. In Sections 5 and 6, we evaluate our algorithm against state of the art methods and review the different anisotropy measures and algorithms proposed using spherical harmonic coefficients and independent elements of the HODT. We show the potential and usefulness of the generalized GA measure for HARDI proposed by Ozarslan et al [29]. We conclude with a discussion of the results and our contributions in Section 7.

2 High Angular Resolution Diffusion Imaging (HARDI)

Diffusion magnetic resonance imaging, introduced in the mid 1980s by Le Bihan et al [19], has become intensely used for the past ten years due to important image acquisition improvement. It is the unique non-invasive technique capable of quantifying the anisotropic diffusion of water in biological tissues such as muscle and brain white matter. Shortly after the first acquisition of images

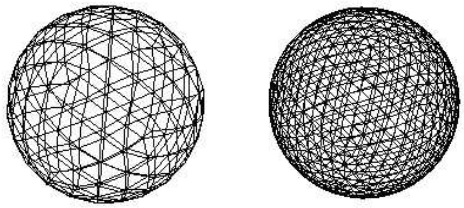

162 points 642 points

Figure 2: Discrete samplings of the sphere for different numbers of gradient directions corresponding to order 3 and order 4 tessellation of the sphere respectively.

characterizing the anisotropic diffusion of water molecules in 1990 [26, 27], Basser et al. proposed the diffusion tensor model [4, 3]. DTI computes the apparent diffusion coefficients (ADC) based on the assumption that the diffusion or Brownian motion of water molecules can be described by a zero-mean Gaussian distribution

$$P(\mathbf{r}) = \left(\frac{1}{(4\pi\tau)^3|\mathbf{D}|}\right)^{\frac{1}{2}} \exp\left(\frac{\mathbf{r}^T\mathbf{D}^{-1}\mathbf{r}}{4\tau}\right). \quad (1)$$

$P(\mathbf{r})$ is the probability that a water molecule starting at a given position in a voxel will have been displaced by some radial vector $\mathbf{r}$ in time τ. The diffusion process is then fully described by a rank-2 diffusion tensor $\mathbf{D}$ which is a positive-definite 3x3 symmetric matrix. Using a minimum of six different encoded gradient directions g, the diffusion tensor can be constructed at each voxel in the volume. The resulting signal attenuation is given by the Stejskal-Tanner equation [37],

$$S(g) = S_0 \exp\left(-bg^T\mathbf{D}g\right) \quad (2)$$

where b is the diffusion weighting factor depending on scanner parameters such as the length and strength of the diffusion gradient and time between diffusion gradient pulses and S_0 is the T2-weighted signal acquired without any diffusion gradients. Numerous methods for estimating and regularizing the diffusion tensor have been proposed [39, 45, 47, 7]. Segmentation and tractography on known fiber bundles with clear anisotropic regions of single fiber bundles work well [20, 21, 22, 23, 24] but the approaches are intrinsically limited and unstable in regions of multiple fibers due to the restrictive assumption of the diffusion tensor model.

In order to better describe the complexity of water motion, a clinically feasible approach, high angular resolution diffusion imaging (HARDI), has been proposed by Tuch et al [43, 40]. At the cost of longer acquisition times, the idea is to sample the sphere in N discrete gradient directions (Fig. 2) and compute the apparent diffusion coefficient (ADC) profile $D(g)$ along each direction [42]. Hence, at each voxel, we have a discrete spherical function with no a priori assumption about the nature of the diffusion process within the voxel. There have been interesting works done recently on alternative ways to obtain complex sub-voxel tissue architecture, such as DSI [46, 40], Q-ball [41],

PASMRI [25]. However, in this paper, we focus on HARDI data and in particular, the development of new and efficient techniques to process noisy spherical data obtained in multiple directions. Several recent approaches have attempted to estimate and investigate properties of noisy spherical data obtained from HARDI [43, 15, 2, 10, 28] to characterize tissues with non-Gaussian diffusion. The problem is to recover a smooth ADC, $D(g)$, close to the true ADC from the measured diffusion MRI noisy signal $S(g)$,

$$S(g) = S_0 \exp\left(-bD(g)\right) \Longrightarrow D(g) = -\frac{1}{b} \ln\left(\frac{S(g)}{S_0}\right). \tag{3}$$

We study the existing methods, discuss their limitations and propose a fast and robust algorithm for ADC profile estimation in the following sections.

3 Apparent Diffusion Coefficient (ADC) Profile Estimation

At each voxel of HARDI data, we have a noisy sampling of the underlying ADC profile describing the diffusion of water molecules within the voxel. In this section, we review tools for analyzing function defined on the sphere and describe state of the art methods for obtaining the underlying ADC profile from discrete noisy samplings. There are two classes of algorithms for ADC profile estimation. The first uses a truncated spherical harmonic series to approximate the function on the sphere [15, 2, 10] whereas the other fits a high order diffusion tensor to the data [28].

3.1 Estimating the ADC Profile with the Spherical Harmonics (SH)

Before discussing the fitting of data to a spherical harmonic series, we first define the spherical harmonics and discuss briefly some of their properties.

3.1.1 Spherical Harmonics (SH)

The spherical harmonics, normally indicated by Y_ℓ^m (ℓ denotes the order and m the phase factor), are a basis for complex functions on the unit sphere satisfying the SH differential equation

$$\frac{1}{\sin\theta}\frac{\partial}{\partial\theta}(\sin\theta\frac{\partial F}{\partial\theta}) + \frac{1}{\sin^2\theta}\frac{\partial^2 F}{\partial\phi^2} + \ell(\ell+1)F = 0, \quad \ell \in Z_+ \tag{4}$$

The first two terms of this equation correspond to the Laplacian in spherical coordinates, also called the three dimensional Laplace-Beltrami operator $\triangle_b$, which is defined by

$$\triangle_b F = \frac{1}{\sin\theta}\frac{\partial}{\partial\theta}(\sin\theta\frac{\partial F}{\partial\theta}) + \frac{1}{\sin^2\theta}\frac{\partial^2 F}{\partial\phi^2}. \tag{5}$$

The Laplace-Beltrami operator is a natural measure of smoothness for functions defined on the unit sphere and has been used in many image processing applications [16, 35, 34]. Furthermore, it is

particularly easy to work with for applications involving the spherical harmonics because, referring to Eq. 4, we know that the spherical harmonics satisfy the relation $\triangle_b Y_\ell^m = -\ell(\ell+1)Y_\ell^m$.

For each nonnegative integer ℓ there are exactly $2\ell+1$ spherical harmonics given by $Y_\ell^{-\ell}, \ldots, Y_\ell^0, \ldots, Y_\ell^\ell$, i.e. $m = -\ell, \ldots, 0, \ldots, \ell$. Explicitly, they are given as follows

$$Y_\ell^m(\theta,\phi) = \sqrt{\frac{2\ell+1}{4\pi}\frac{(\ell-m)!}{(\ell+m)!}} P_\ell^m(\cos\theta) e^{im\phi} \tag{6}$$

where (θ,ϕ) obey physics convention ($\theta \in [0,\pi], \phi \in [0,2\pi)$) and P_ℓ^m is an associated Legendre polynomial, which can be obtained analytically from the following set of equations,

$$P_\ell(x) = \frac{1}{2^\ell \ell!}\left(\frac{d}{dx}\right)^\ell (x^2-1)^\ell \tag{7}$$

$$P_\ell^m(x) = (-1)^m (1-x^2)^{\frac{m}{2}} \left(\frac{d}{dx}\right)^m P_\ell(x), \quad m \geq 0 \tag{8}$$

$$P_\ell^{-m}(x) = (-1)^m \frac{(\ell-m)!}{(\ell+m)!} P_\ell^m(x) \tag{9}$$

The normalization factor in Eq. 6 is chosen so that the spherical harmonics form an orthonormal set of functions with respect to the inner product

$$< f, g >= \int_\Omega f^* g \tag{10}$$

where integration over Ω denotes integration over the unit sphere, and f^* denotes the complex conjugate of f. Finally, observe that with respect to the transformation

$$T : (\theta,\phi) \rightarrow (\pi-\theta, \phi+\pi),$$

the spherical harmonics have the following very simple behavior,

$$Y_\ell^m(T(\theta,\phi)) = \begin{cases} Y_\ell^m(\theta,\phi), & \text{if } \ell \text{ even} \\ -Y_\ell^m(\theta,\phi), & \text{if } \ell \text{ odd} \end{cases} \tag{11}$$

In other words, the even order spherical harmonics are antipodally symmetric, while the odd order spherical harmonics are antipodally antisymmetric. We will be using these important properties in the development of our regularization algorithm.

3.1.2 Methods for Fitting Spherical Data with SH Series

The set of spherical harmonics forms an orthonormal basis for all functions on the unit sphere. High order spherical harmonics correspond to high frequency modes of the unit sphere, and thus a

truncated spherical harmonic series can be effectively used to fit relatively smooth functions. Since they form a basis, any spherical function $x : S^2 \to C$ can be written as

$$x(\theta,\phi) = \sum_{\ell=0}^{\infty} \sum_{m=-\ell}^{\ell} c_\ell^m Y_\ell^m(\theta,\phi). \tag{12}$$

Moreover, due to orthonormality of the SH basis, the coefficients of the SH series c_ℓ^m can be calculated by forming the inner product of x with the spherical harmonics,

$$c_\ell^m = \langle x(\theta,\phi), Y_\ell^m(\theta,\phi)\rangle = \int_0^{2\pi}\int_0^{\pi} x(\theta,\phi) Y_\ell^m(\theta,\phi)\sin\theta d\theta d\phi \tag{13}$$

This idea was first used to fit the ADC profile obtained from HARDI data by Frank in [15] where the function x is replaced by the discrete sampling of the diffusivities, $D(g)$ (Eq. 3) . Frank performs the direct discretization of the integrals. This is a computationally poor method to obtain the coefficients and recent salient work by Alexander et al [2] use a least-squares method to solve for the unknowns. The least-squares method was first proposed in the vision community for the parametrization of closed surfaces for 3D shape description by Brechbuhler et al [6]. Letting n_s be the number of discrete point on the sphere, n_b the number of SH used in the approximation ($n_s \gg n_b$), $X = (x_1, ..., x_{n_s})^T$, $C = (c_0^0, c_1^{-1}, c_1^0, \ldots)^T$ and

$$B = \begin{bmatrix} Y_0^0(\theta_1,\phi_1) & Y_1^{-1}(\theta_1,\phi_1) & \cdots & Y_{n_b}^{n_b}(\theta_1,\phi_1) \\ Y_0^0(\theta_2,\phi_2) & Y_1^{-1}(\theta_2,\phi_2) & \cdots & Y_{n_b}^{n_b}(\theta_2,\phi_2) \\ \vdots & \vdots & \ddots & \vdots \\ Y_0^0(\theta_{n_s},\phi_{n_s}) & Y_1^{-1}(\theta_{n_s},\phi_{n_s}) & \cdots & Y_{n_b}^{n_b}(\theta_{n_s},\phi_{n_s}) \end{bmatrix}, \tag{14}$$

we want the spherical harmonic series that passes nearest to the discrete samplings on the sphere. Hence, $X = BC + E$, where the error vector E should be small. This system of overdetermined equations is solved with least-squares sum over the columns of E by minimizing $||X - BC||^2$ yielding

$$\boxed{C = (B^T B)^{-1} B^T X}. \tag{15}$$

The vector C of spherical harmonic coefficients gives the best-fitting truncated series to the ADC profile. The estimated ADC profile is thus recovered by evaluating the following equation,

$$D(\theta,\phi) = \sum_{\ell=0}^{n_b} \sum_{m=-\ell}^{\ell} c_\ell^m Y_\ell^m(\theta,\phi) \tag{16}$$

for any (θ,ϕ) outside the discrete measurements X or in the discrete case, by simple matrix multiplication $D(g) = BC$. Though this works fairly well so long as noise is kept small, we propose, in Section 4, a more general fitting procedure that take advantage of the properties of spherical harmonics and the Laplace-Beltrami operator to quantify the smoothness of spherical functions. Before doing so, we review the relationship between the spherical harmonic series of order-ℓ and the higher order diffusion tensor of rank-ℓ.

3.2 Fitting the ADC Profile with a High Order Diffusion Tensor (HODT)

In [28], instead of fitting the ADC profile with a rank-2 tensor, the diffusivities are expressed in terms of a high order Cartesian tensor $\mathbf{D}$

$$D(g) = \sum_{i_1=1}^{3} \sum_{i_2=1}^{3} ... \sum_{i_\ell=1}^{3} \mathbf{D}_{i_1 i_2 ... i_\ell} g_{i_1} g_{i_2} ... g_{i_\ell} \tag{17}$$

where the $\mathbf{D}_{i_1 i_2 ... i_\ell}$'s are the elements of $\mathbf{D}$ and the g_i's are the components of the unit vector specifying the direction of the applied diffusion gradient

$$g = \begin{pmatrix} g_1 \\ g_2 \\ g_3 \end{pmatrix} = \begin{pmatrix} \sin\theta\cos\phi \\ \sin\theta\sin\phi \\ \cos\theta \end{pmatrix} \tag{18}$$

Replacing $g^T \mathbf{D} g$ in the standard Stejskal-Tanner equation (Eq. 2) with $D(g)$ as found in Eq. 17 leads to a generalized Stejskal-Tanner equation. This model assumes no a priori knowledge of the diffusion profile. However, in order to use Eq. 17, we must assume that a rank-ℓ tensor is sufficient to determine the apparent diffusion coefficient profile, $D(g)$. Given this assumption, it is possible to simplify the problem further by exploiting the properties of the diffusion tensor.

The diffusion tensor must be totally symmetric, which means that the diffusion tensor remains the same under any permutation of indices. Because of this symmetry, we can then define a subset of diffusion tensor elements, that we call the set of independent elements, which represents a choice of the smallest subset sufficient to fully characterize the diffusion tensor. Each independent element is representative of the equivalence class generated by unique permutations of the indices of that independent element. As the diffusion tensor is totally symmetric, each element in an equivalence class has to take the same value. The number of elements in an equivalence class is called the multiplicity. Each distinct equivalence class is thus characterized by the number of x's, y's and z's in its indices, and the sum of these has to be the rank of the tensor. Thus, the problem of determining the total number of independent elements is then equivalent to finding the number of possible combinations of two integers such that their sum is less than or equal to the rank of the tensor. This is a straightforward calculation from which the number of independent elements of a rank-ℓ tensor is

$$n_b = \sum_{n=1}^{\ell+1} n = \frac{1}{2}(\ell+1)(\ell+2) \tag{19}$$

This greatly simplifies the problem since, for large ℓ the total number of elements is much larger than the number of independent elements ($3^\ell \gg n_b$). Using the arguments above, the authors of [28] rewrite the expression for D(g) in a more compact form. In order to do this, they need to know the multiplicity of each independent element of the HODT. Consider the group of all permutations of ℓ elements, S_ℓ. The subgroup of unique permutations is equal to S_ℓ modulo the subgroup of all permutations that do not change the indices. Note that permuting only the x's (or y's or z's) does not create a distinct set of indices. With a little more algebra, the subgroup of permutations fixing

the indices turns out to be the product of permutations of x's, permutations of y's and permutations of z's. Thus, the multiplicity μ of a component of a rank-ℓ tensor is

$$\mu = \frac{|S_\ell|}{|S_x| \cdot |S_y| \cdot |S_z|} = \frac{\ell!}{n_x! n_y! n_z!} \tag{20}$$

where S_x, S_y, and S_z are respectively the permutation groups of the x, y, and z indices, and n_x, n_y, and n_z are just the number of x, y, and z indices contained in the subscript of the given independent element. With this information, much of Eq. 17 becomes redundant, and we can reduce it to

$$D(g) = \sum_{k=1}^{n_b} \mu_k \mathbf{D}_k \prod_{p=1}^{\ell} g_{k(p)}, \tag{21}$$

where D_k is the k^{th} independent element of the tensor, μ_k is its corresponding multiplicity, and $g_{k(p)}$ gives the component of the gradient direction g corresponding to the p^{th} index of the k^{th} independent element of the tensor. To illustrate this simplification, consider the vector of independent elements of a rank-2 diffusion tensor $\mathbf{D} = (\ \mathbf{D}_{xx}\ \mathbf{D}_{xy}\ \mathbf{D}_{xz}\ \mathbf{D}_{yy}\ \mathbf{D}_{yz}\ \mathbf{D}_{zz}\ )^T$ which has multiplicity vector $\mu = (1\ 2\ 2\ 1\ 2\ 1)^T$. We then have

$$\begin{aligned}
D(g) &= \sum_{i_1 \in \{x,y,z\}} \sum_{i_2 \in \{x,y,z\}} D_{i_1 i_2} g_{i_1} g_{i_2} \\
&= g_x^2 \mathbf{D}_{xx} + g_y^2 \mathbf{D}_{yy} + g_z^2 \mathbf{D}_{zz} + g_x g_y \mathbf{D}_{xy} + g_y g_x \mathbf{D}_{yx} \\
&\quad + g_x g_z \mathbf{D}_{xz} + g_z g_x \mathbf{D}_{zx} + g_y g_z \mathbf{D}_{yz} + g_z g_y \mathbf{D}_{zy} \\
&= g_x^2 \mathbf{D}_{xx} + 2 g_x g_y \mathbf{D}_{xy} + + 2 g_x g_z \mathbf{D}_{xz} + g_y^2 \mathbf{D}_{yy} + 2 g_y g_z \mathbf{D}_{yz} + g_z^2 \mathbf{D}_{zz} \\
&= \sum_{k=1}^{6} \mu_k \mathbf{D}_k \prod_{p=1}^{2} g_{k(p)}
\end{aligned}$$

which illustrates the simplification. Combining Eq. 3 and Eq. 21, we have

$$D(g) = \sum_{k=1}^{n_b} \mu_k \mathbf{D}_k \prod_{p=1}^{\ell} g_{k(p)} = -\frac{1}{b} \log\left(\frac{S(g)}{S_0}\right). \tag{22}$$

Ozarslan et al [28, 29] fit the ADC profile with a HODT using linear regression with processing routines written in IDL (Research Systems, Inc., Boulder, CO). We are not sure of the exact routines used in this procedure but we have implemented a standard linear regression with least-squares fitting as described in the previous section. We want $\mathbf{D}$, the vector of HODT independent elements, such that

$$D(\theta_i, \phi_i) = \sum_{k=1}^{n_b} \mu_k \mathbf{D}_k \prod_{p=1}^{\ell} g_{k(p)}(\theta_i, \phi_i). \tag{23}$$

Letting X be the diffusivities $D(\theta_i, \phi_i)$, and

$$R = \begin{bmatrix} \mu_1 \prod_{p=1}^{\ell} g_{1(p)}(\theta_1, \phi_1) & \cdots & \mu_{n_b} \prod_{p=1}^{\ell} g_{n_b(p)}(\theta_1, \phi_1) \\ \vdots & \ddots & \vdots \\ \mu_1 \prod_{p=1}^{\ell} g_{1(p)}(\theta_{n_s}, \phi_{n_s}) & \cdots & \mu_{n_b} \prod_{p=1}^{\ell} g_{n_b(p)}(\theta_{n_s}, \phi_{n_s}) \end{bmatrix}, \tag{24}$$

we define an error term E' so that $X + E' = R\mathbf{D}$. We seek to minimize the quantity $E'^T E'$ using the same techniques described previously. We then obtain the expansion for the HODT

$$\boxed{\mathbf{D} = (R^T R)^{-1} R^T X}. \tag{25}$$

The estimated ADC profile is thus recovered by evaluating

$$D(\theta, \phi) = \sum_{k=1}^{n_b} \mu_k \mathbf{D}_k \prod_{p=1}^{\ell} g_{k(p)}(\theta, \phi) \tag{26}$$

for any (θ, ϕ) outside the discrete measurements X or in the discrete case, by simple matrix multiplication $D(g) = R\mathbf{D}$.

It is important to mention that it is physically impossible to have negative diffusivities because the ADC profile describes the diffusion of water molecules, which is a positive process. The proposed linear regression does not guarantee the positive definiteness of $\mathbf{D}$. Moreover, the method does not have a smoothing or regularization parameter and will therefore be sensitive to noise.

4 Fitting HODTs to HARDI Data Using Spherical Harmonics

4.1 A Regularization Algorithm for ADC Profile Estimation

The first step in our method is to take raw HARDI ADC profile data and fit it to a truncated spherical harmonic series. There are five primary constraints on the diffusivity profile that need to be considered in the optimization of this fit. It must be 1) real, 2) antipodally symmetric, 3) positive, 4) relatively smooth, and 5) in close agreement with the measured data. Constraints 1), 2) and 3) are physical constraints due to the nature of diffusion MRI acquisition. The first two are relatively straightforward to deal with, in that they can be ensured by a simple choice of modified spherical harmonic basis. In order to impose the antipodal symmetry constraint on the expansion, we consider only spherical harmonics of even degree. As mentioned before, spherical harmonics of odd order are antipodally anti-symmetric, while spherical harmonics of even order are antipodally symmetric. In order to impose the real-valued constraint, we consider a basis of real linear combinations of the spherical harmonics as the basis. In this modified basis, the real-valued constraint on the ADC profile can be taken into consideration simply by optimizing the fit over the set of real coefficients. The

$$Y_1 = Y_0^0$$

$$Y_2 = \frac{\sqrt{2}}{2}\left(Y_2^2 + Y_2^{-2}\right), \qquad Y_3 = \frac{\sqrt{2}}{2}\left(-Y_2^1 + Y_2^{-1}\right)$$

$$Y_4 = Y_2^0$$

$$Y_5 = \frac{i\sqrt{2}}{2}\left(Y_2^1 + Y_2^{-1}\right), \qquad Y_6 = \frac{i\sqrt{2}}{2}\left(-Y_2^2 + Y_2^{-2}\right)$$

$$Y_7 = \frac{\sqrt{2}}{2}\left(Y_4^4 + Y_4^{-4}\right), \qquad Y_8 = \frac{\sqrt{2}}{2}\left(-Y_4^3 + Y_4^{-3}\right)$$

$$Y_9 = \frac{\sqrt{2}}{2}\left(Y_4^2 + Y_4^{-2}\right), \qquad Y_{10} = \frac{\sqrt{2}}{2}\left(-Y_4^1 + Y_4^{-1}\right)$$

$$Y_{11} = Y_4^0$$

$$Y_{12} = \frac{i\sqrt{2}}{2}\left(Y_4^1 + Y_4^{-1}\right), \quad Y_{13} = \frac{i\sqrt{2}}{2}\left(-Y_4^2 + Y_4^{-2}\right)$$

$$Y_{14} = \frac{i\sqrt{2}}{2}\left(Y_4^3 + Y_4^{-3}\right), \quad Y_{15} = \frac{i\sqrt{2}}{2}\left(-Y_4^4 + Y_4^{-4}\right)$$

Table 1: Modified spherical harmonics basis of order 4

idea of modeling the ADC profile with physical constraints was proposed in Chen et al [10] where they also use only even order SHs and construct a constrained minimization problem forcing the ADC profile estimate to be real and positive. Our approach is slightly different in that we make sure that we add a smoothing term as discussed later, and also enforce the real-valued constraint simply by our choice of a modified spherical harmonic basis, rather than by implementing a complicated constrained minimization routine.

For $\ell = 0, 2, 4, \ldots, \ell_{max}$ and $m = -\ell, \ldots, 0, \ldots, \ell$, our modified basis is

$$Y_j = \begin{cases} \frac{\sqrt{2}}{2}((-1)^m Y_\ell^m + Y_\ell^{-m}), & \text{if } j(\ell,m) = \frac{\ell^2+\ell+2}{2} + m \text{ and } -\ell \le m < 0 \\ Y_l^0, & \text{if } j(\ell,m) = \frac{\ell^2+\ell+2}{2} + m \text{ and } m = 0 \\ \frac{\sqrt{2}i}{2}((-1)^{m+1} Y_\ell^m + Y_\ell^{-m}), & \text{if } j(\ell,m) = \frac{\ell^2+\ell+2}{2} + m \text{ and } 0 < m \le \ell \end{cases} \tag{27}$$

Table 1 shows the rank-4 basis as an example. Note that there are exactly $n_b = \frac{1}{2}(\ell+1)(\ell+2)$ ($n_b = 15$ when $\ell = 4$) terms in the SH series of order ℓ and the constants in front of the composed terms ensure orthonormality with respect to the inner product of Eq. 10. For the rest of the paper, $Y_1, \ldots, Y_{n_b}$ will refer to the modified spherical harmonic basis. Now, we can reformulate the approximation of the ADC profile as the problem of determining the coefficients c_j in

$$D(\theta_i, \phi_i) = \sum_{j=1}^{n_b} c_j Y_j(\theta_i, \phi_i). \tag{28}$$

As in Section 3.1.2, we use noisy HARDI data sampled at a set of n_s points (θ_i, ϕ_i) on the sphere, the i^{th} element of which will be denoted by x(θ_i, ϕ_i). Therefore, we have a similar set of equations for the coefficients c_j,

$$x(\theta_i, \phi_i) = \sum_{j=1}^{n_b} c_j Y_j(\theta_i, \phi_i) \qquad \text{for } \ 1 \leq \mathrm{i} \leq \mathrm{n_s} \tag{29}$$

From HARDI data, we usually have more discrete samplings on the sphere than terms in the modified SH basis ($n_s \gg n_b$) and thus, we can write the equations given above as an overdetermined linear system $X + E = BC$, as before and now with the B matrix constructed with the modified spherical harmonics basis. At this point, instead of performing a simple least-squared minimization from which we obtain the result given in Eq. 15, we want to add regularization to our fitting procedure. We propose to find the solution that minimizes the sum of the previously discussed squared error term and the new smoothness term. We define a measure of the deviation from smoothness E of a function f defined on the unit sphere as

$$E(f) = \int_\Omega (\triangle_b f)^2, \tag{30}$$

where integration over Ω denotes integration over the unit sphere and $\triangle_b$ is the Laplace-Beltrami operator. The Laplace-Beltrami operator is a natural measure of smoothness for functions defined on the unit sphere and as stated before, we know that the spherical harmonics satisfy the relation $\triangle_b Y_\ell^m = -\ell(\ell+1)Y_\ell^m$. Note that this relation also holds for our modified SH basis. As a result, the above functional can be rewritten straightforwardly in terms of the coefficient vector C as follows:

$$\begin{aligned} E(f) &= \int_\Omega \triangle_b \left(\sum_p c_p Y_p \right) \triangle_b \left(\sum_q c_q Y_q \right) \\ &= \sum_{j=1}^{n_b} c_j^2 \ell_j^2 (\ell_j + 1)^2 \qquad \text{(orthonormality of the modified basis)} \\ &= C^T L C, \end{aligned} \tag{31}$$

where L is simply the n_b x n_b matrix with entries $\ell_j^2(\ell_j + 1)^2$ along the diagonal. Therefore, the quantity we wish to minimize can be expressed in matrix form as

$$M(C) = (BC - X)^T (BC - X) + \lambda C^T L C, \tag{32}$$

where λ is a variable weighting factor on the regularization term. The coefficient vector minimizing this expression can then be determined just as in the standard least-squares fit ($\lambda = 0$), by setting each of the $\frac{\partial M}{\partial c_j} = 0$, from which we obtain the generalized expression for the desired spherical harmonic series coefficient vector

$$\boxed{C = (B^T B + \lambda L)^{-1} B^T X}. \tag{33}$$

The estimated ADC profile is thus recovered by evaluating

$$D(\theta,\phi) = \sum_{j=1}^{n_b} c_j Y_j(\theta,\phi) \tag{34}$$

for any (θ,ϕ) outside the discrete measurements X or in the discrete case, by simple matrix multiplication $D(g) = BC$.

Intuitively, this approach penalizes an approximation function for having higher order terms in its modified SH series. Therefore, higher order terms will only be included in the fit if they significantly improve the overall accuracy of the approximation. This eliminates most of the high order terms due to noise while leaving those that are necessary to describe the underlying function. However, obtaining this balance depends on choosing a good value for the parameter λ. We use the *L-curve* numerical method [17] and experimental simulations to determine the best smoothing parameter. This will be described in Section 5. Note that a variation on the above derivation will hold in other geometries if a proper basis of functions is chosen.

4.2 From SH Coeffi cients to HODT Coeffi cients

We now explicitly derive the correspondence between coefficients of the modified spherical harmonic series and the independent elements of the high order diffusion tensor. Ozarslan et al [28] showed the analytical relationship between the SH coefficients and the independent elements of the HODT. Conceptually, they showed that evaluating the ADC in terms of a HODT is equivalent to fitting the ADC with a spherical harmonics series. Thus, it is possible to define a general linear transformation to go from one to the other.

By Appendix A, we know that both the even order spherical harmonics up to order ℓ, and the rank-ℓ HODT polynomials restricted to the sphere, are bases for the same function space. Therefore, given a vector of HODT coefficients $\mathbf{D}$, we know that there exists a vector C of spherical harmonic coefficients such that

$$\sum_{i=1}^{n_b} c_j Y_j(\mathbf{g}) = \sum_{k=1}^{n_b} \mathbf{D}_k \mu_k \prod_{p=1}^{\ell} g_{k(p)}(\mathbf{g}). \tag{35}$$

Now, multiplying both sides of this equation by Y_m and integrating over the unit sphere, we obtain by the orthonormality of the spherical harmonics

$$c_m = \sum_{k=1}^{n_b} \mathbf{D}_k \int_\Omega \mu_k \prod_{p=1}^{\ell} g_{k(p)}(\mathbf{g}) Y_m(\mathbf{g}) d\mathbf{g} \tag{36}$$

This straightforwardly translates into matrix form as

$$C = M\mathbf{D} \tag{37}$$

where

$$M = \begin{bmatrix} \mu_1 \int_\Omega \prod_{p=1}^{\ell} g_{1(p)} Y_1(\mathbf{g}) d\mathbf{g} & \dots & \mu_{n_b} \int_\Omega \prod_{p=1}^{\ell} g_{n_b(p)} Y_1(\mathbf{g}) d\mathbf{g} \\ \vdots & \ddots & \vdots \\ \mu_1 \int_\Omega \prod_{p=1}^{\ell} g_{1(p)} Y_{n_b}(\mathbf{g}) d\mathbf{g} & \dots & \mu_{n_b} \int_\Omega \prod_{p=1}^{\ell} g_{n_b(p)} Y_{n_b}(\mathbf{g}) d\mathbf{g} \end{bmatrix}. \quad (38)$$

Since both sets of functions form bases for the same space, the linear transformation M between them is a change of basis matrix, and is thus invertible (proof in Appendix A). Therefore, given a vector C of SH coefficients, we can use M^{-1} to compute the corresponding vector of HODT coefficients. This argument, exploiting the orthonormality of the spherical harmonics, provides a more computationally generalizable way of determining the matrix M than the algorithm suggested by the inductive proof of Appendix A. We thus have obtained a linear mapping between the spherical harmonic coefficients and HODT independent elements. Fig. 3 and Fig. 4 illustrate the transformation procedure analytically for the example of the rank-2 diffusion tensor. When using the standard spherical harmonic basis (Fig. 3), we obtain the exact same relationship presented by Ozarslan et al [28]. In Fig. 4, we derive the same relations using our modified spherical harmonic basis. Note that all matrix entries are *real*, which captures the real-valued constraint on the problem.

Putting everything together, i.e. combining Eqs. 33 and 37, the linear transformation taking the raw HARDI data sampling X to the vector $\mathbf{D}$ of HODT independent coefficients using our spherical harmonic regularization step is

$$\boxed{\mathbf{D} = M^{-1}(B^T B + \lambda L)^{-1} B^T X}. \quad (39)$$

The technique is fast because it only involves linear transformations and more importantly, matrices B(Eq. 14) and M(Eq. 38) are the same for all voxels in the data set and need only be computed once. Therefore, we have obtained a real and symmetric high order diffusion tensor and the estimated ADC profile can be recovered, as in Section 4.2 by evaluating Eq. 26 for any (θ, ϕ) outside the discrete measurements X or in the discrete case, by simple matrix multiplication $D(g) = R\mathbf{D}$.

Note that the physical positivity constraint of the ADC profile is not ensured in this derivation. One must make sure that $D(g) = g^T \mathbf{D} g \geq 0$. In implementing our algorithm, we found that this was rarely relevant at reasonable noise levels, as our algorithm gave everywhere positive results without being explicitly constrained to do so. However, in the standard rank-2 DTI problem, methods have been proposed to deal with data where some of the estimated tensors step out of the positive-definite matrix space [38, 9, 23]. In [38], a simple numerical extension of the PDE-based approach for tensor estimation is proposed to preserve the positive-definite property of each tensor. At each numerical iteration involved with solving the PDE, tensors are diagonalized and reprojected into the space of symmetric semi-positive space by setting the negative eigenvalues to zero. Hence, the approach requires a spectral decomposition of the tensors at each step which is slow. In [9], the problem is better posed mathematically and PDE's are derived to preserve discontinuities of constrained matrix-valued images. A similar gradient descent approach on the manifold of multivariate normal distributions, which shows promising results, is used in [23] with a Riemannian metric. The question

$\ell = 2$, using standard spherical harmonics basis:

$$\text{SH basis } Y = \begin{pmatrix} \frac{1}{2\sqrt{\pi}} \\ \frac{1}{4}\sqrt{\frac{15}{2\pi}}\sin^2\theta e^{-2i\phi} \\ \frac{1}{2}\sqrt{\frac{15}{2\pi}}\sin\theta\cos\theta e^{-i\phi} \\ \frac{1}{4}\sqrt{\frac{5}{2\pi}}(3\cos^2\theta - 1) \\ -\frac{1}{2}\sqrt{\frac{15}{2\pi}}\sin\theta\cos\theta e^{i\phi} \\ \frac{1}{4}\sqrt{\frac{15}{2\pi}}\sin^2\theta e^{2i\phi} \end{pmatrix} \quad \mathbf{D} = \begin{pmatrix} D_{xx} \\ D_{xy} \\ D_{xz} \\ D_{yy} \\ D_{yz} \\ D_{zz} \end{pmatrix}$$

$$M = \begin{pmatrix} \sqrt{\frac{4\pi}{9}} & 0 & 0 & \sqrt{\frac{4\pi}{9}} & 0 & \sqrt{\frac{4\pi}{9}} \\ \sqrt{\frac{2\pi}{15}} & \sqrt{\frac{8\pi}{15}}i & 0 & -\sqrt{\frac{2\pi}{15}} & 0 & 0 \\ 0 & 0 & \sqrt{\frac{8\pi}{15}} & 0 & \sqrt{\frac{8\pi}{15}}i & 0 \\ -\sqrt{\frac{4\pi}{45}} & 0 & 0 & -\sqrt{\frac{4\pi}{45}} & 0 & \sqrt{\frac{16\pi}{45}} \\ 0 & 0 & -\sqrt{\frac{8\pi}{15}} & 0 & \sqrt{\frac{8\pi}{15}}i & 0 \\ \sqrt{\frac{2\pi}{15}} & -\sqrt{\frac{8\pi}{15}}i & 0 & -\sqrt{\frac{2\pi}{15}} & 0 & 0 \end{pmatrix}$$

$$M\mathbf{D} = C = \begin{pmatrix} \sqrt{\frac{4\pi}{9}}(D_{xx} + D_{yy} + D_{zz}) \\ \sqrt{\frac{2\pi}{15}}(D_{xx} - D_{yy} + 2iD_{xy}) \\ \sqrt{\frac{8\pi}{15}}(D_{xz} + iD_{yz}) \\ -\sqrt{\frac{4\pi}{45}}(D_{xx} + D_{yy} - 2D_{zz}) \\ \sqrt{\frac{8\pi}{15}}(iD_{yz} - D_{xz}) \\ \sqrt{\frac{2\pi}{15}}(D_{xx} - D_{yy} - 2iD_{xy}) \end{pmatrix}$$

Figure 3: Illustration of transformation M from independent elements of the HODT, $\mathbf{D}$, to our modified SH series coefficients, C, for a rank-2 tensor. Using the standard spherical harmonics basis, we obtain the exact same expression as presented in [28].

$\ell = 2$, using modified spherical harmonics basis (Eq. 27):

$$\text{SH basis } = Y = \begin{pmatrix} \frac{1}{2\sqrt{\pi}} \\ \frac{1}{4}\sqrt{\frac{15}{\pi}}\sin^2\theta\cos(2\phi) \\ \frac{1}{2}\sqrt{\frac{15}{\pi}}\sin\theta\cos\theta\cos\phi \\ \frac{1}{4}\sqrt{\frac{5}{2\pi}}(3\cos^2\theta - 1) \\ \frac{1}{2}\sqrt{\frac{15}{\pi}}\sin\theta\cos\theta\sin\phi \\ \frac{1}{4}\sqrt{\frac{15}{\pi}}\sin^2\theta\sin(2\phi) \end{pmatrix} \quad \mathbf{D} = \begin{pmatrix} D_{xx} \\ D_{xy} \\ D_{xz} \\ D_{yy} \\ D_{yz} \\ D_{zz} \end{pmatrix}$$

$$M = \begin{pmatrix} \sqrt{\frac{4\pi}{9}} & 0 & 0 & \sqrt{\frac{4\pi}{9}} & 0 & \sqrt{\frac{4\pi}{9}} \\ \sqrt{\frac{4\pi}{15}} & 0 & 0 & -\sqrt{\frac{4\pi}{15}} & 0 & 0 \\ 0 & 0 & \sqrt{\frac{16\pi}{15}} & 0 & 0 & 0 \\ -\sqrt{\frac{4\pi}{45}} & 0 & 0 & -\sqrt{\frac{4\pi}{45}} & 0 & \sqrt{\frac{16\pi}{45}} \\ 0 & 0 & 0 & 0 & \sqrt{\frac{16\pi}{15}} & 0 \\ 0 & \sqrt{\frac{16\pi}{15}} & 0 & 0 & 0 & 0 \end{pmatrix}$$

$$M\mathbf{D} = C = \begin{pmatrix} \sqrt{\frac{4\pi}{9}}(D_{xx} + D_{yy} + D_{zz}) \\ \sqrt{\frac{4\pi}{15}}(D_{xx} - D_{yy}) \\ \sqrt{\frac{16\pi}{15}}D_{xz} \\ -\sqrt{\frac{4\pi}{45}}(D_{xx} + D_{yy} - 2D_{zz}) \\ \sqrt{\frac{16\pi}{15}}D_{yz} \\ \sqrt{\frac{16\pi}{15}}D_{xy} \end{pmatrix}$$

Figure 4: Illustration of transformation M from independent elements of the HODT, $\mathbf{D}$, to our modified SH coefficients, C, for a rank-2 tensor. Using our modified SH basis, the coefficients of M are always real.

shema.eps shema.ps shema.eps.gz shema.ps.gz shema.eps.Z

Figure 5: Sketch of our regularization algorithm. It illustrates the main parts and equations of the method and in particular, it shows the bridge between spherical harmonic coefficients and independent coefficients of the high order diffusion tensor.

of how to extend this approach in the space of high order tensors is open and goes beyond the scope of this report. We cannot simply use the idea of [38] because, in general, high order tensors cannot always be decomposed. However, it is part of current work to look for numerical schemes that impose $D(g)$ to always be positive.

The ultimate goal when estimating and denoising the diffusivity profile is to use it to infer the underlying diffusion process. This is commonly done using anisotropy measures defined on whatever set of coefficients is used to describe the ADC profile. With our algorithm, we can either work directly with the spherical harmonic coefficients or choose to use the coefficients of the high order diffusion tensor. The method and the main equations are clearly sketched in Fig. 5 where it is shown how spherical harmonic coefficients and high order tensor elements are linked.

5 Synthetic Data Experiments

In the following sections, we first evaluate the performance of our ADC profile fitting procedure compared with other techniques in the literature and secondly test the different HARDI anisotropy measures on both synthetic and real data. For the synthetic tests of our algorithm, we used the multi-tensor model for multiple fibers, as described in [2]. This model assumes that single fiber responses can be described by a Gaussian (rank-2 tensor) and that the tissue in a voxel with more than one fiber is simply composed of multiple Gaussian fibers that do not exchange molecules. With these assumptions, the signal obtained is

$$S(g) = S_0 \sum_{i=1}^{n} p_i e^{-bg^T \mathbf{D}_i g} \tag{40}$$

where n is the number of fibers, p_i is the proportion of tissue in the voxel that corresponds to the i^{th} fiber ($\sum_{i=1}^{n} p_i = 1$), $\mathbf{D}_i$ is the second order diffusion tensor corresponding to the i^{th} fiber, g is the direction of the applied diffusion gradient and b is a constant determined by the diffusion MRI scanner. A fairly standard b-value for medical imaging is $b = 3000 s/mm^2$. In [2], Alexander et al perform experiments with many fiber variations between the standard white-matter diffusion tensor with eigenvalues $[1700,\ 200,\ 200] \cdot 10^{-6} mm^2/s$ and the isotropic tensor with equal eigenvalues $[700,\ 700,\ 700] \cdot 10^{-6} mm^2/s$. In our experiment, we choose to only consider the white-matter fiber of the brain. Given this assumption, any $\mathbf{D}_i$ can be constructed with the use of rotation matrices

from the diagonalized matrix

$$\mathbf{D} = 10^{-6} \cdot \begin{pmatrix} 1700 & 0 & 0 \\ 0 & 200 & 0 \\ 0 & 0 & 200 \end{pmatrix} \tag{41}$$

This makes computation using this model relatively straightforward. We are trying to obtain the diffusivity profile, however, rather than the signal itself, so we cannot directly use this approach. Instead, we wish to find D(g) such that

$$S(g) = S_0 e^{-bD(g)} \tag{42}$$

We find this by simply setting Eq. 40 equal to Eq. 42 to obtain the result that D(g) is

$$D(g) = -\frac{1}{b} \ln \left(\frac{S(g)}{S_0} \right) = -\frac{1}{b} \ln \left(\sum_{i=1}^{n} p_i e^{-bg^T D_i g} \right) \tag{43}$$

To test our model on various fiber distributions we generate discrete samplings on the sphere. We used the standard 81 point HARDI sampling of the hemisphere with almost equally sparse gradients g to obtain a spherical function with 162 points as illustrated in Fig. 2. We generate voxels with 1, 2, or 3 randomly distributed fibers or with an isotropic distribution. With 162 points on the sphere, the resolution between gradient directions is about 16 degrees and thus, we impose a minimum angle of 45 degrees between fibers for better discrimination. Finally, we add Rician noise (complex Gaussian noise) [33, 32] with a standard deviation of $\sigma = 1/35$ to the raw signal (Eq. 42) such that the unweighted signal S_0 has a signal to noise ratio (SNR) of 35, a typical value for current medical scanners [2, 40].

The multi-tensor model has also been used for synthetic data experiments by other authors (e.g. Tuch [41]) and it is worth mentioning that there exists another popular synthetic data generation model used in other works [44, 14, 29]. In this formulation, Soderman and Jonsson [36] suppose that fibers are perfect cylinders and that water molecules are confined to diffuse within the walls of these cylinders. In the presence of multiple fibers, the signal attenuation from the cylinders is additive. This gives a more physically-based mixture model but is less realistic than the multi-tensor model that corresponds more closely to empirical fiber data. In any case, the approaches have the same model-selection and fitting problems [1].

5.1 Quantitative Comparison

In order to test the effectiveness of recovering the original (without noise) synthetic diffusivity profile from noisy sparse data measurements, we compare our algorithm (sketched in Fig. 5) qualitatively and quantitatively to methods presented in Section 3. To do so, we estimate the HODT from the noisy sampled ADC profile and then compute the estimated true ADC profile with Eq. 26. For our algorithm, $\mathbf{D}$ is obtained from Eq. 39. For the Ozarslan et al [28] linear regression (LR) method, we get $\mathbf{D}$ from Eq. 25. Finally, we also use the un-smoothed SH technique ($\lambda = 0$) of Eq. 15 that resembles estimation approaches proposed by Frank [15] and is essentially the same as the method

		1 fiber test with λ (x10^{-3})					
	LR	0	6	12	100	**300**	500
mean	0.083	0.083	0.071	0.068	0.052	**0.051**	0.054
std	0.064	0.063	0.051	0.046	0.036	**0.035**	0.037
		2 fiber test with λ (x10^{-3})					
	LR	0	3	**6**	9	12	15
mean	0.076	0.075	0.070	**0.069**	0.070	0.070	0.072
std	0.052	0.052	0.043	**0.041**	0.040	0.041	0.042
		3 fiber test with λ (x10^{-3})					
	LR	0	6	9	12	**15**	100
mean	0.092	0.092	0.049	0.040	0.034	**0.031**	0.057
std	0.037	0.037	0.028	0.026	0.025	**0.025**	0.026
		random fiber test with λ (x10^{-3})					
	LR	0	6	12	**100**	200	300
mean	0.078	0.078	0.068	0.065	**0.064**	0.067	0.070
std	0.054	0.055	0.045	0.043	**0.042**	0.044	0.045

Table 2: Numerical simulation to find the best regularization weight λ for ADC profile fitting and comparison with Ozarslan et al linear regression (LR) method. We show the mean and standard deviation (std) of the squared difference between the true ADC profile and the estimated profile. The best values for each test are in bold fonts.

used in Alexander et al [2], except that they use a different spherical harmonics basis. In the latter case, we need to apply our transformation matrix M^{-1}(Eq. 38) to obtain $\mathbf{D}$. In the following tables, the error measures recorded are the mean and standard deviation (std) of the error vector E'' specified by the point-wise squared difference between points on the estimated ADC points and points on the true (without noise) ADC profiles

$$E''_i = (D_{\text{true}}(\theta_i, \phi_i) - D(\theta_i, \phi_i))^2. \tag{44}$$

5.1.1 Effect of the λ-Regularization Weight

We want to find the optimal λ for our regularization algorithm. This is not a trivial task because there are different optimal λ's depending on the underlying fiber distribution. In fact, in the cases of 1 or no fibers, a high order tensor formulation is unnecessary and thus, it is expected to obtain a higher optimal λ for these cases than for multiple fiber diffusion. To find the optimal regularization parameter, we use the *L-curve* method of [17]. In our least-squares minimization problem, we need to plot the data errors $||BC - X||^2$ against the regularization term $C^T LC$ while varying λ. Hence, we simulate random 1, 2, and 3 fiber distribution, we incrementally vary $\lambda \in [0, 0.5]$ and record the pair $(||BC - X||^2, C^T LC)$. As seen in Fig. 6, this gives a set of noisy points(green dots) to which we can fit a *best* curve that will be our L-curve. We choose a 4^{th} order polynomial least-squares fit, which models the data well. The optimal λ is then the point on the curve with maximum curvature,

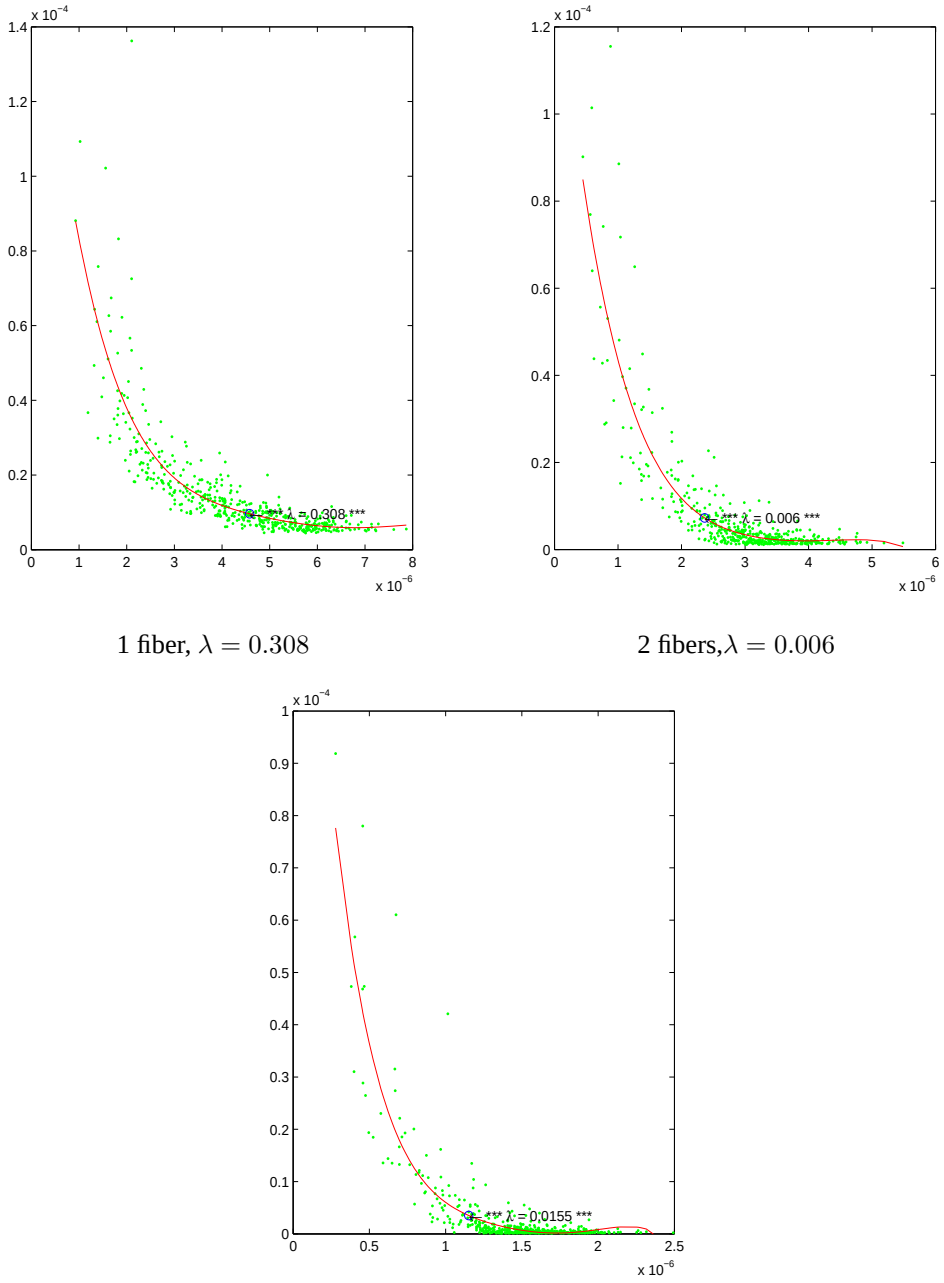

1 fiber, $\lambda = 0.308$

2 fibers,$\lambda = 0.006$

3 fibers,$\lambda = 0.0155$

Figure 6: L-curves for 1, 2 and 3 fibers with optimal λ circled. The green points are the discrete points in the experiment and the red curve is the least-squares best fit with a 4^{th} order polynomial.

1 fiber test

	LR	$\lambda = 0$	$\lambda = 0.006$
mean	0.083	0.083	0.071
std	0.064	0.063	0.051

2 fiber test

	LR	$\lambda = 0$	$\lambda = 0.006$
mean	0.076	0.075	0.069
std	0.052	0.052	0.041

3 fiber test

	LR	$\lambda = 0$	$\lambda = 0.006$
mean	0.092	0.092	0.049
std	0.037	0.037	0.028

random fiber test

	LR	$\lambda = 0$	$\lambda = 0.006$
mean	0.078	0.078	0.068
std	0.054	0.055	0.045

Table 3: Comparison between LR method, spherical harmonics series with no regularization and our approach with smoothing parameter set to $\lambda = 0.006$. For all tests, $\lambda = 0.006$ performs better than LR of [28] and SH series with $\lambda = 0$ of [15, 2].

which is the location that separates the flatter and more vertical parts of the graph. These are where the solution is dominated by regularization errors and perturbation errors respectively. We plot the L-curves for 1, 2 and 3 randomly distributed fibers in Fig. 6. We show the set of measured points, the fitted L-curve and indicate the optimal λ with a circle.

In order to verify the L-curve optimal values, we simulate in the same way as above, 10000 synthetic diffusivity profiles of 1, 2 and 3 fibers and compute the Ozarslan et al linear regression (LR) and our algorithm's estimations for different values of λ. For each test, we compute the mean and standard deviation (std) of the squared error between the true and estimated ADC profile (Eq. 44). From Table 2, there are several expected observations that one can make. Firstly, from the first two columns, we note that the linear regression fit of a HODT and the SH series fit with no regularization ($\lambda = 0$) are the same up to a very small numerical error. As previously discussed, this is to be expected because the two models are equivalent and there exists a direct change of basis transformation between the two. Secondly, as observed with the L-curve, single fiber voxels are optimally fit with a larger λ than in the multiple fiber voxels. This occurs because in the case of a single fiber, higher order estimation is unnecessary. Intuitively, a large λ cancels the effect of high order tensor terms so that the model is closer to a rank-2 tensor formulation. However, as soon as we have more structure, as in the cases of 2 or 3 fibers, λ of 0.006 and 0.015 are best, respectively. This is expected as we need to maintain significant contribution from higher order terms in order to accurately fit multi-fiber ADC profiles. In the random case, a λ of 0.1 gives the best results. These best numerical λ values closely agree with the L-curve points of maximum curvature. Finally, from Table 3, we note that in all cases, $\lambda = 0.006$ performs better than both linear regression and the SH fit with $\lambda = 0$. Moreover, $\lambda = 0.006$ is also the optimal value for the L-curve in the case of 2 fibers. Therefore, for the rest of the experiments, we set $\lambda = 0.006$ based on the assumption that it is critical to robustly distinguish multiple fiber diffusion from single fiber diffusion, especially between single and two fiber distributions.

Qualitatively, Fig. 7 illustrates how we obtain a smoother ADC profile estimation that visually agrees with results from Table 3. Our regularized tensor estimation gives a diffusivity profile closer

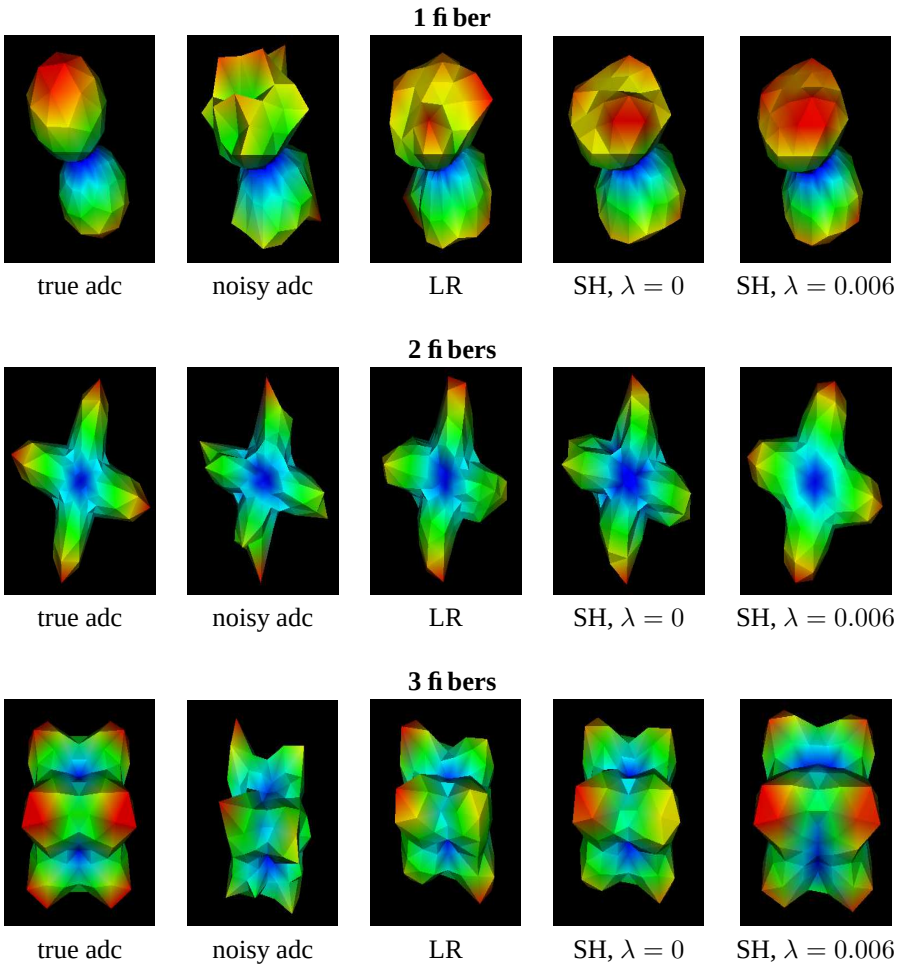

Figure 7: Visualizing the ADC profile fitting procedure. We have in row 1 the ADC profile for a single fiber, in row 2 the ADC profile for two orthogonal fibers and row 3 is for three orthogonal fibers. Qualitatively, the last column gives the best approximation of the true ADC profile.

to the true ADC profile without noise than other methods considered. Here, instead of visualizing the data on the unit sphere, we have stretched the surface mesh with respect to each ADC profile value $D(\theta_i, \phi_i)$. The color map is red for high values and blue for low ADC profile values.

5.2 Anisotropy Measures

We now explore the different measures found in the literature that attempt to characterize anisotropy from high order approximations of the ADC profile. There are two classes of anisotropy measures for HARDI data. One is defined on the coefficients a SH series (Frank [15], Alexander et al [2], Chen et al [10]) and the other on the independent elements of a HODT (Ozarslan et al [28]). We implement these important measures from the literature and compare their behavior. We also study their ability to identify the underlying diffusion process. On synthetic data, we demonstrate that our algorithm can differentiate between isotropic diffusion, 1-fiber diffusion and multi-fiber diffusion.

5.2.1 Frank and Chen et al Measures

The two measures found in the Frank and Chen et al papers are similar and based on SH coefficients. Frank [15] proposes a simple Fractional Multifiber Index (FMI) that is the ratio of the sum of squared high order coefficients coefficients over order-2 coefficients. It is given by

$$FMI = \frac{\sum\limits_{\{j:\ell\geq 4\}} |c_j|^2}{\sum\limits_{\{j:\ell=2\}} |c_j|^2} = \frac{\sum\limits_{j=7}^{n_b} |c_j|^2}{\sum\limits_{j=2}^{6} |c_j|^2} \tag{45}$$

where $n_b = \frac{1}{2}(\ell+1)(\ell+2)$ is the number of elements in the truncated SH series.

Chen et al [10] claim that the FMI ratio is insufficient to separate isotropic, 1-fiber and multi-fiber behavior within a voxel. They decide to introduce the variance of the ADC profile $D(g)$ about its mean value into the characterization of the underlying diffusive behavior with the following ratios

$$R_0 = \frac{|c_0|}{\sum\limits_{\forall j} |c_j|} \quad , \quad R_2 = \frac{\sum\limits_{\{j:\ell=2\}} |c_j|}{\sum\limits_{\forall j} |c_j|} \quad , \quad R_{multi} = \frac{\sum\limits_{\{j:\ell\geq 4\}} |c_j|}{\sum\limits_{\forall j} |c_j|} \quad .$$

In their paper, they restrict the maximum number of fibers in a voxel to 2 and they use a rank-4 approximation. Hence, they only use R_0 and R_2 ratios. We generalize their approach for more than two directions and use a rank-8 estimation. R_{multi} is a natural multi-fiber ratio extension. These anisotropy ratios can be used to formulate an algorithm to distinguish between isotropic, 1-fiber and multi-fiber diffusion. It is roughly sketched in Fig. 8. We carefully pick the thresholds in these algorithms by performing tests on synthetic data to obtain the best results.

5.2.2 Alexander et al Measure

Alexander et al. use ANOVA [2] to determine if truncating the series at a higher order as opposed to a lower order significantly changes the fit to the model data. The *F-test* is

$$F(M_2, M_\ell) = \frac{(N - p_\ell - 1)(Var(M_\ell) - Var(M_2))}{(p_\ell - p_2)E(M_\ell)}$$

```
if R0 is large OR Variance(ADC) is small
        ISOTROPY

else if R2 is large OR Variance(ADC) is large
        if Rmulti is large
            MULTI FIBER
        else
            SINGLE FIBER

else if Rmutli is large
        MULTI FIBER
```

Figure 8: Rough sketch of the anisotropy algorithm from Chen et al [10] generalized for more than two directions and higher order approximations.

where E is the mean squared error between the true ADC profile and the estimated ADC profile at the N sampled points and p_i is the number of free parameters in model M_i. In our case, the lower order model is M_2 (order-2 diffusion tensor) and we test it against higher order approximation models M_ℓ for $\ell = 4, 6, 8$. We then have, $N = 162$, $p_2 = 6$ and $p_\ell = \frac{1}{2}(\ell + 1)(\ell + 2)$. In [2], ANOVA is used to dynamically choose the order of the SH series approximation.

5.2.3 Results of Anisotropy Measures from SH Series

Our goal is to correctly classify synthetic noisy data, generated as described in Section 5, into three classes: 0 for isotropic diffusion, 1 for 1-fiber anisotropic diffusion and 2 for multi-fiber diffusion, i.e. diffusion corresponding to either 2 or more fibers. To do so, we attempt to find the best thresholds that separate the different measures into these three classes. We test the robustness of the classifications under rank change. We analyze the behavior of the measures and note the different characteristics.

From Table 4, we see that Chen et al and ANOVA measures behave similarly and are more stable than Frank's measure. The advantage of Chen's algorithm is that it involves well-chosen SH coefficient ratios and the variance of the ADC profile which makes it more robust to noise and less sensitive to the threshold selection. In fact, we do not have adapt thresholds between tests when changing λ and the rank of the HODT. This is not the case with ANOVA. It is also important to note the better performance of our regularization procedure with a non-zero λ used in conjunction with the Chen et al and the ANOVA measures. This clearly illustrates the added value brought by our method described in Section 4. This is because the estimated ADC profile is smoother, and hence, the SH coefficient ratios incorporate less noise. On the other hand, for Frank's measure, we note that it performs better when $\lambda = 0$. This is not surprising because of the nature of the ratio and in particular, because the numerator depends only on high order terms of the SH series. With a non-

	FMI		Chen		ANOVA	
	$\lambda = 0$	$\lambda = 0.006$	$\lambda = 0$	$\lambda = 0.006$	$\lambda = 0$	$\lambda = 0.006$
$\ell = 8$	93.1%	85.1%	83.2%	96.0%	91.7%	94.8%
$\ell = 6$	93.1%	84.2%	89.1%	97.0%	90.9%	94.5%
$\ell = 4$	83.2%	82.2%	93.1%	97.0%	88.7%	91.1%
$\ell = 2$			54.4%	54.5%		

Table 4: Classification success percentages using anisotropy measures. We test the effects of varying λ and rank. Note the errors with a rank-2 approximation in Chen's column. FMI and ANOVA measures make no sense in the $\ell = 2$ case.

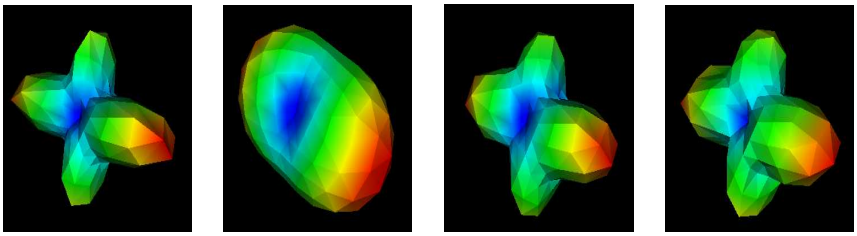

true $\ell = 2$ $\ell = 4$ $\ell = 8$

Figure 9: Rank-2 approximation fails to describe non-Gaussian diffusion.

zero λ, the coefficients of higher order are penalized, and therefore have lower values than without a smoothing term. The ratio is thus not designed to be used with our method.

In all cases, the classification errors occur for two specific types of synthetic data. First, when there are two fibers very close to one another (≈ 45 degrees), we can obtain the misclassification where the true number of fibers is underdetermined by one. This is a limitation due to the angular resolution between discrete samplings on the sphere and also the noise present in the data. Secondly, we observe that a noisy distribution of three fibers close to orthogonal behaves like isotropic diffusion.

Finally, from both column 2 of Table 4 and Fig. 9, we clearly see that a rank-2 diffusion tensor model is not sufficient to describe the ADC profile and detect multi-fiber diffusion. In this particular case, all anisotropy classifications detect multi-fiber diffusion with $\ell = 4, 6$ and 8 but detect single fiber diffusion with the $\ell = 2$ approximation. For the $\ell = 2$ approximation, the peaks of the true ADC profile are lost and it looks like a flat ellipsoid.

5.2.4 Generalized Anisotropy Measure

Ozarslan et al. in their recent article [29] generalize the well-known DTI FA (fractional anisotropy) measure for HARDI data fitted with high order tensors. Their generalized anisotropy (GA) measure is based on the generalization of the trace, mean diffusivity and the variance of the normalized

diffusivity of high order tensors. The trace of a rank-2 tensor $\mathbf{D}$ is given by the sum of its eigenvalues, and if it is antipodally symmetric, it can be expressed as the integral over the unit hemisphere Ω of its quadratic form

$$\text{trace}(\mathbf{D}) = \frac{3}{2\pi}\int_{\Omega} g^T \mathbf{D} g dg.$$

Thus, it is possible to generalize this trace expression for any antipodally symmetric spherical function f and obtain the generalized trace "gentr",

$$\text{gentr}(f(g)) = \frac{3}{2\pi}\int_{\Omega} f(g) dg.$$

Inspired by the rank-2 tensor case where FA is expressed in the new form

$$FA = \sqrt{\frac{1}{2}\left(3 - \frac{1}{\text{trace}(\mathbf{D}_N^2)}\right)}$$

related to the variance of the eigenvalues of the normalized tensor ($\mathbf{D}_N = \mathbf{D}/\text{trace}(\mathbf{D})$) in the case that $\mathbf{D}$ is diagonalized, Ozarslan et al propose a generalized version using the variance of the generalized trace of the normalized diffusivities $\mathbf{D}_N(g)$. This generalized variance is defined as

$$V = \frac{1}{3}\left(\text{gentr}(\mathbf{D}_N(g)^2) - \frac{1}{3}\right), \qquad \text{where} \qquad \mathbf{D}_N(g) = \frac{D(g)}{\text{gentr}(D(g))} \tag{46}$$

The last step of the GA measure is to make sure it is restricted to the interval $[0, 1)$ by choosing a monotonic function that maps the interval $[0, \infty)$ to $[0, 1)$. This choice seems to be relatively "ad-hoc" and dependent on the dataset to be processed. The final generalized anisotropy (GA) measure is defined as

$$GA = 1 - \frac{1}{1 + (250V)^{e(V)}}, \qquad \text{where} \qquad e(V) = 1 + \frac{1}{1 + 5000V}. \tag{47}$$

We have skipped many important details in the GA derivation and we strongly refer the reader to the article [29] for the complete description. Contrary to ratios/measures/algorithms proposed from spherical harmonic coefficients reviewed in the previous section, GA has the property of being scaled between 0 and 1 and does not assume any specific approximation order. It can be quickly and easily visualized to obtain cues on the anisotropy regions, just as FA in the DTI case.

Even though the exact values are different because we use a different synthetic data generation, we are able, in Table 5, to reproduce the same behaviors of the GA measure published by Ozarslan et al. In particular, for a single fiber, the measures are almost independent of the rank being used for the estimation (first row in table). However, GA measures are significantly higher for rank-{4,6,8} than for the rank-2 model when there are multiple fibers. There is also an overlap in GA values between diffusion in 3-fiber distribution and isotropic diffusion. It is in these cases that the rank-2 model is unsatisfying. We also note similar GA values and behaviors between our regularization algorithm and our implementation of Ozarslan's linear regression.

	Our method ($\lambda = 0.006$) , LR			
	$\ell = 2$	$\ell = 4$	$\ell = 6$	$\ell = 8$
1 fiber	0.92,0.92	0.92,0.92	0.92,0.92	0.92,0.92
2 fibers	0.64,0.65	0.71,0.73	0.72,0.73	0.70,0.71
3 fibers	0.09,0.09	0.19,0.23	0.20,0.13	0.10, 0.09
isotropic	0.09,0.09	0.09,0.10	0.09,0.09	8x10^{-4},0.01

Table 5: Mean GA measure over 10000 simulated ADC profiles. We show the mean GA calculated from our algorithm and Ozarslan's linear regression (LR) method. We observe similar overall behaviors as the ones reported in [29].

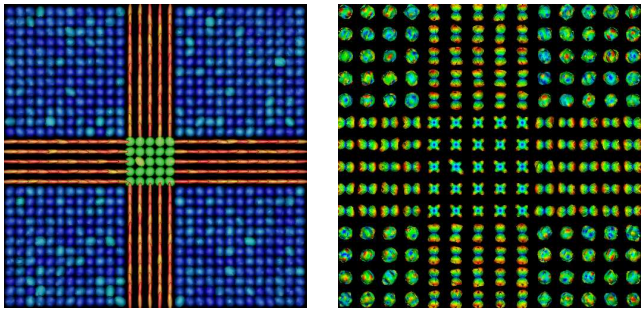

Figure 10: Two orthogonal fiber bundles crossing. In the top left, red ellipsoids are oriented along the fiber bundles, green ellipsoids are flat in the crossing area and blue ellipsoids are close to spheres in the background. We show the field of ADC profiles in the top right where we see multiple peaks in the crossing. The last row shows the FA and GA anisotropy maps. The anisotropy is much lower in the crossing area in both cases.

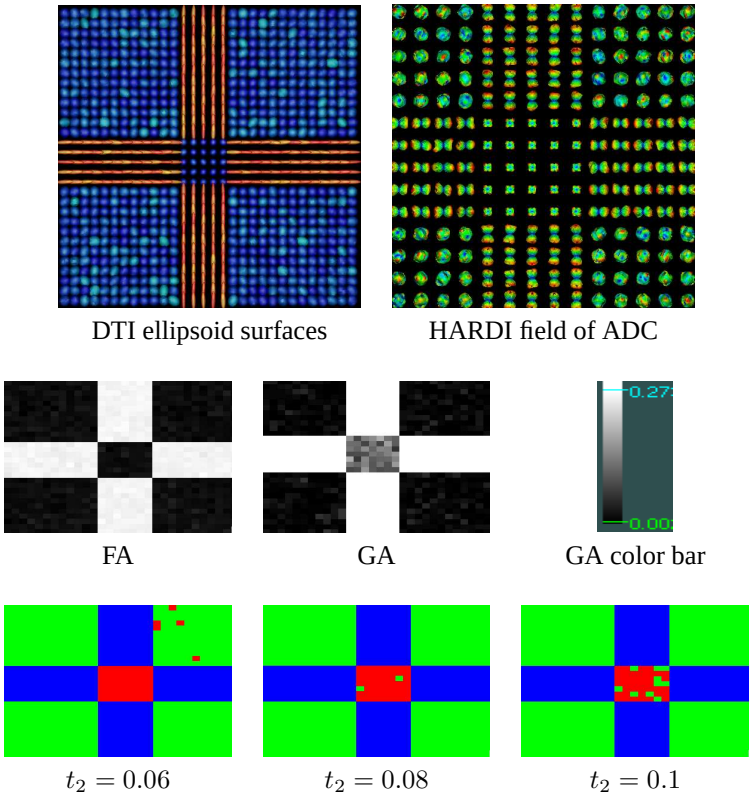

Figure 11: Three orthogonal fiber bundles crossing. In the top left is the field of surface ellipsoids corresponding to rank-2 diffusion tensor estimation and in the top right is the field of approximated ADC profiles. Red ellipsoids are elongated in the directions of fiber orientation and blue ellipsoids represent isotropic tensors in the crossing area and background. In the HARDI field there is a difference between the background ADC profiles and those in the crossing area. The second row clearly shows the ability of GA to pick up the crossing area whereas the FA map is in the same range as the background in that region. We can thus attempt to threshold the GA to classify the diffusion. The last row illustrates the effect of varying the t_2 threshold value in the classification process. green := isotropic, blue := 1 fiber, red := multi-fiber. Some voxels are incorrectly classified.

	Spherical Harmonics		Linear Regression
	$\lambda = 0.006$	$\lambda = 0$	
$\ell = 8$	99.8%	99.9%	99.3%
$\ell = 6$	99.8%	99.6%	99.2%
$\ell = 4$	100%	99.9%	99.6%
$\ell = 2$	78.6%	77.6%	78.1%

Table 6: Classification with GA. 10000 random fiber test with our algorithm and Ozarslan's linear regression method.

Furthermore, due to the consistent behavior of GA values, (i.e. small variation in GA measure among fiber distributions of the same number of fibers), we can push the experiment further and attempt to classify the different underlying synthetic fiber distributions. The thresholds are considerably easier to choose than with the measures using spherical harmonics presented earlier. Using the mean and standard deviation of the GA from Table 5, we choose thresholds $t_1 = 0.90$ and $t_2 = 0.08$. Our classification procedure is then simple. If $GA > t_1$ we classify the voxel as 1-fiber anisotropic diffusion, else if $GA < t_2$ we have isotropic diffusion and otherwise, we mark the voxel as a multi-fiber distribution.

We again generate tests with 10000 randomly distributed 1-fiber, 2-fiber, 3-fiber and isotropic diffusion single voxels. In order to validate the approach on a field of noisy spherical functions, we also extend our single voxel synthetic generation to construct a noisy high angular resolution 30x30 slice with a 5x5 crossing configuration in the center. We perform one experiment with two and another with three orthogonal fibers crossing. Table 6 and Fig. 11 show the success of the classification results on synthetic data. Detection of fiber distributions is more stable and better with GA than with measures from spherical harmonics. GA values clearly discriminate the different diffusion processes except for rank-2 approximation where the overlap between three-fiber and isotropic diffusion causes many misclassifications. For rank-$\{4, 6, 8\}$, the only errors made are when there are 3-fiber distributions with signals very close to that of isotropic diffusion. In Figs. 10 and 11 we also include the DTI ellipsoid surfaces which clearly illustrate the planar and isotropic tensors in the crossing of the respective tests. These were computed using standard least-squares fit from all discrete high angular measures. The color map is blue for isotropic, green for planar and red for anisotropic ellipsoids. We also see the FA map limitations in the crossing areas. In particular, note that for the three crossing patterns in Fig. 11, the FA measure is in the same range as the background whereas the GA map is able to distinguish the multi-fiber diffusion process.

5.2.5 Cumulative Residual Entropy (CRE)

We now review the CRE index [31], a measure that is very different from the measures presented so far. CRE is based on a probability measure computed from the full ADC profile sampling whereas previous measures are defined from the coefficients of either the SH or HODT vector describing the ADC profile. CRE is an information theory measure with interesting properties and similar behavior

	Our method with $\lambda = 0.006$			
	$\ell = 2$	$\ell = 4$	$\ell = 6$	$\ell = 8$
1 fiber	0.13	0.17	0.16	0.16
2 fibers	0.096	0.096	0.097	0.097
3 fibers	0.0044	0.049	0.047	0.047
isotropic	0.0042	0.0067	0.0078	0.0096

Table 7: CRE experiment. In left table, we show the behavior of the entropy index on 10000 synthetic ADC profiles. The right table shows the classification results when changing the rank.

in practice as GA. Chen et al [11] proposed this measure to overcome the limitations of their previous anisotropy algorithm (Fig. 8). It reduces the number of parameters required to characterize the diffusion process to two [11]. The CRE of a continuous random variable $A \in \mathbf{R}$ is defined as

$$CRE(A) = -\int_{R^+} P(A > \sigma) \log P(A > \sigma) d\sigma. \tag{48}$$

The weak theorem of CRE [31] states that in the discrete case, where we have discrete samples of A, CRE converges to the true CRE (as the number of samplings goes to infinity). This is the main advantage of CRE over the popular Shannon entropy ($H(A) = \sum_{i=1}^{N} p(A_i) \log P(A_i)$) for which this property does not hold. Thus, in [11], CRE is computed from the discrete estimated sampling of the ADC profile $D(g)$ as:

$$CRE(e^{-bD(g)}) = -\sum_{i=1}^{M} P(e^{-bD(g)} > \sigma_i) \log P(e^{-bD(g)} > \sigma_i) \triangle\sigma_i, \tag{49}$$

where $\{\sigma_1 < \sigma_2 < ... < \sigma_M\}$ is defined over the range of $e^{-bD(g)}$ at each voxel and $\triangle_i = \sigma_{i+1} - \sigma_i$ is the absolute difference between two adjacent $e^{-bD(g)}$. One again, we compute the average values of CRE for 0, 1, 2 and 3 fiber distributions from 10000 synthetic $D(g)$ profiles with $M = 1000$, as in [11]. From Table 7, we observe the same overall anisotropy index behavior as obtained from the GA measure. In fact, if we attempt a classification like in the previous section, it is true that two thresholds are enough to classify the synthetic diffusion process. The success rate is very high and in the same range as Table 6. CRE has the advantage of being better theoretically founded and simpler to compute than GA. However, as it will be discussed in the real data experiment, CRE has the same limitations as the GA measure for characterizing diffusion on real data experiments. On the biological phantom, thresholding the measure is not enough to robustly seperate the crossing region from the 1-fiber parts. Despite this, among all tested anisotropy measures for HARDI data, CRE and GA are the most consistent and perform the best. In the context of this report, if we only consider anisotropy measures computed from coefficients of ADC profiles, GA is the one with the most potential. Therefore, for the real data validation, we choose to use GA.

6 Real Data Experiment

6.1 A Biological Phantom

First, we test our algorithm on a biological phantom, Fig 12. It was produced by Campbell et al at the McConnel Brain Imaging Center and Montreal Neurological Institute [7, 8] and was created from two excised Sprague-Dawley rat spinal cords embedded in 2% agar. A high angular resolution dataset was acquired using 90 gradient directions and the q-ball protocol ([41]) with $b = 3000$. The baseline T1-weighted image illustrating the ground truth configurations of the fibers is seen in the top left of Fig.12. We also compare the ellipsoid surfaces obtained from the standard DTI least-squares fit using all 90 directions against the ADC profile computed with our regularized spherical harmonic algorithm. The ellipsoids and ADC profiles are overlaid on the computed GA map. A rank-8 estimation with $\lambda = 0.006$ is used. As expected, the DTI ellipsoid surfaces are planar or tend to be spherical in the crossing area whereas the more complex high order estimation of the ADC profile recover multiple peaks for voxels in that region. Moreover, even though the GA map has slightly noisy background, it recovers both fiber bundles and the measure is different in the crossing than in certain straight single fiber parts. However, contrary to the synthetic data characterization, the GA difference between 1- and 2-fiber regions is not clear enough to fully distinguish the two with simple thresholding. This is also case for the CRE measure (not shown here).

6.2 Human Brain HARDI Data

Secondly, we test our method on a real human brain. Diffusion weighted images were acquired at the Center for Magnetic Resonance Research, University of Minnesota, on a 3 Tesla Siemens Magneton Trio whole-body scanner. We used 81 gradient directions on the hemisphere with 3 repetitions per direction, each with a b-factor of $b = 1000\ s/mm^2$, $TR = 5100s$ and $TE = 109ms$. The voxel size was a $3mm^3$ cube and there were 24, 64x64 slices.

As described in Tuch's thesis [40], normalizing the ADC profile is of great importance for increasing the visual angular contrast of real data. In particular, [[40], Fig. 8.4] illustrates the enhancement of the maxima and minima when the diffusion coefficients are normalized to the interval $[0, 1]$. In this paper, we also have normalized the real data ADC profile in order to emphasize the peaks, i.e. obtain a sharper ADC profile. Otherwise, the diffusivity profiles are visually too close to a sphere and the GA measurements are very close to isotropic.

We have selected 1-fiber and multi-fiber ADC profiles from voxels in the corpus callosum and the corticospinal tract to illustrate the performance of our regularization algorithm on real data. Fig. 13 shows some of the results. We include the FA and GA scalar measures. From the GA maps of the rat biological phantom and human brain dataset, we see that classification on real data is a much more difficult task than the synthetic data experiments where the noisy generated signal is more homogeneous and GA statistics are easily computed. On real data, one has to manually select regions with known crossings and regions with strong single fiber anisotropy to analyze the corresponding GA measure behavior. Due to noise and partial volume effects there is too much overlap between diffusion process classes. However, we observe that the real data normalized ADC profiles have very similar shapes and properties as compared to our synthetic data. Even though we

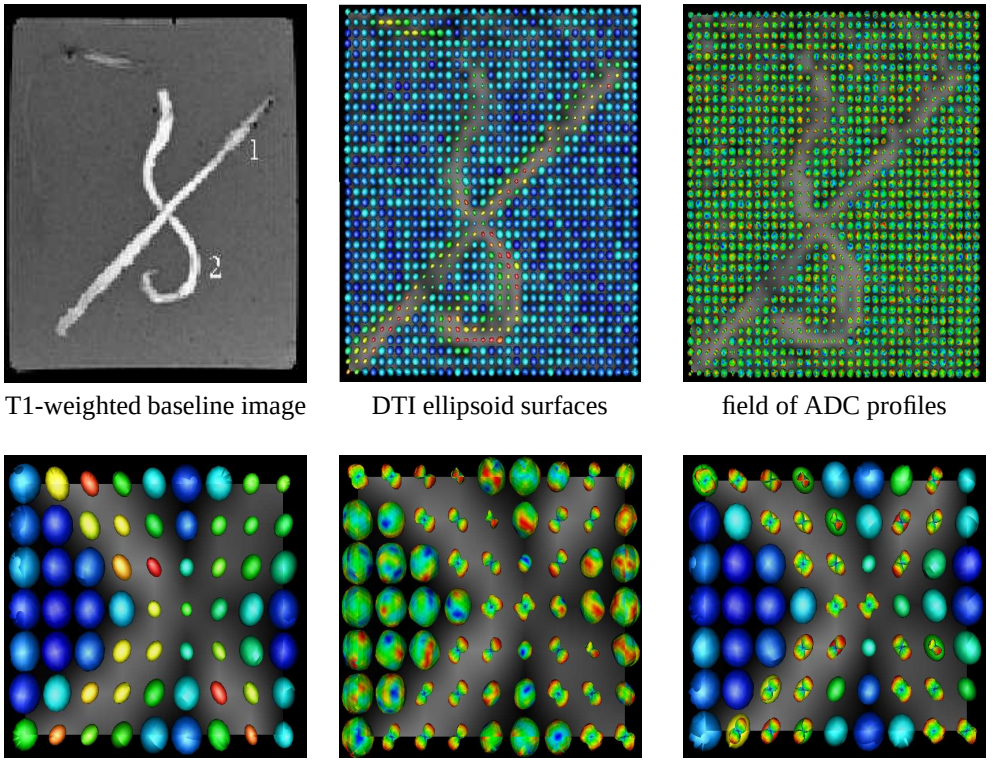

Figure 12: Biological phantom produced at the McConnel Brain Imaging Center [7, 8]. We show the baseline T1-weighted image as well as the fields of DTI ellipsoids and estimated ADC profiles on the whole phantom overlaid on the GA map. Focusing on the crossing area, the DTI ellipsoids tend to be flat (greenish) and spherical (blueish) whereas the ADC profiles clearly have multiple peaks compared to the single fiber bundle area. Recall that maxima of ADC profiles do not correspond to fiber orientation. The ADC profiles are scaled by the GA measure to enhance visual contrast between foreground and background.

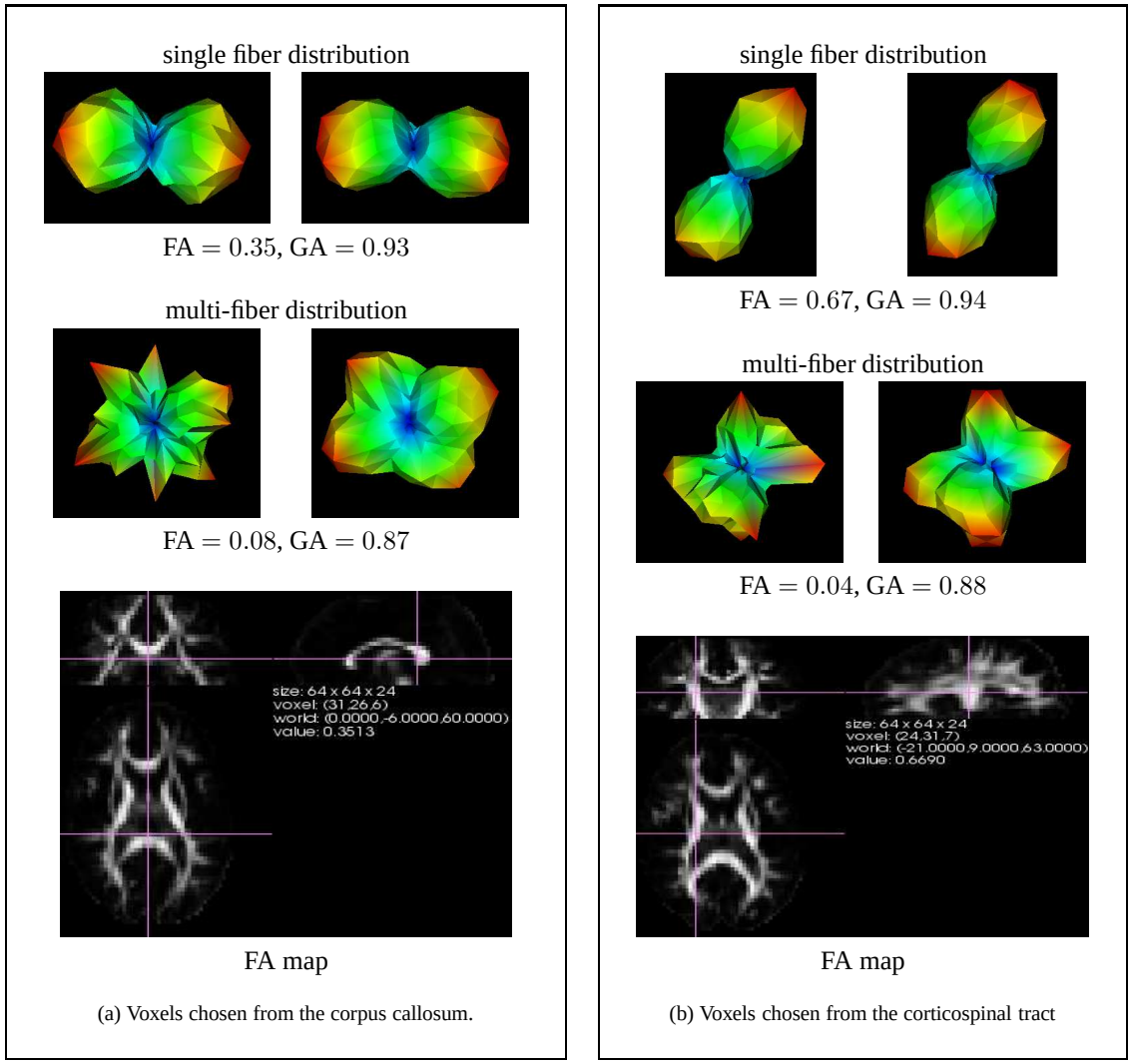

(a) Voxels chosen from the corpus callosum.

(b) Voxels chosen from the corticospinal tract

Figure 13: ADC profiles selected from real data voxels in the corpus callosum and the corticospinal tract. The left column of each sub-figure represents the real profile and the right column is the estimated ADC profile from our regularization algorithm. We report the corresponding FA and GA measures for each and include the FA map with the region of interest marked with a pink overlaid cross.

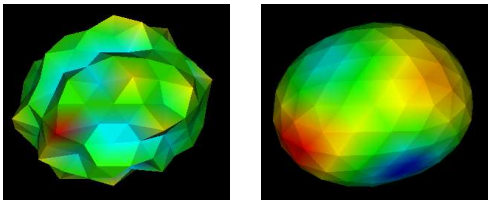

ADC profile $\ell = 4$

Figure 14: Read data ADC profile of a voxel in gray matter.

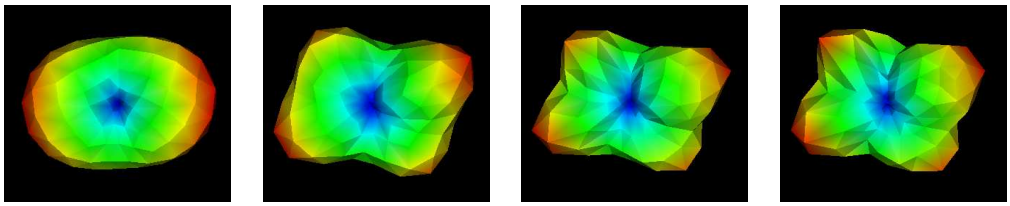

$\ell = 2$ $\ell = 4$ $\ell = 6$ $\ell = 8$

Figure 15: ADC profile at different ranks for the fiber crossing in the corpus callosum of Fig. 13(a).

do not believe one can simply threshold the real data GA map to classify the diffusion process, one can make better use of the GA than FA scalar measure to look for multiple fibers crossing. Visual inspection of the peaks of the ADC profile in the small regions of interest show agreement with neuroanatomy knowledge (Fig. 13) of single and multiple fiber bundles.

In Fig. 14 we have chosen a voxel in the gray matter to illustrate an example of a noisy isotropic ADC profile, and Fig. 15 well-illustrates the limitations of the rank-2 diffusion tensor model. In this case, the estimated ADC profile surface averages the multiple peaks of the true ADC profile and produces a planar ADC profile.

Finally, we reproduce a similar figure as Tuch's in [41, Fig. 12-f] from the genu of the corpus callosum. This region is known to have multiple fibers crossing. We thus observe a lower FA than that found in strong anisotropic areas and a stronger GA value in the range corresponding to 2 or 3 fibers in Table 5. If one locally thresholds this region of interest, the obtained classification provides some valuable information. The multi-fiber regions in red clearly stand out and we can thus identify areas of transition between single (blue) and multiple fiber diffusion. Although not shown here, a very similar classification can be obtained from the CRE measure[1].

[1] In [11, Fig.5], Chen et al obtain a two-fiber classification that strangely occurs mostly on the boundary of white-matter and gray-matter. This figure is unexpected and looks incorrect as it does not pick up known regions of multiple crossings such as areas presented in [41] and Fig. 16.

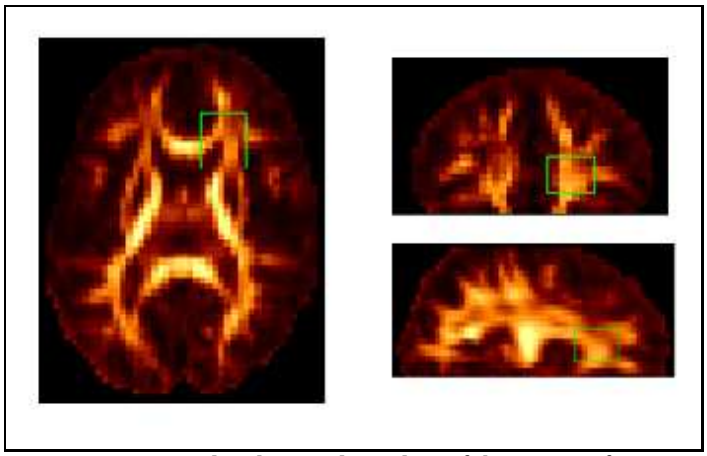

Transverse, coronal and sagittal FA slice of the region of interest

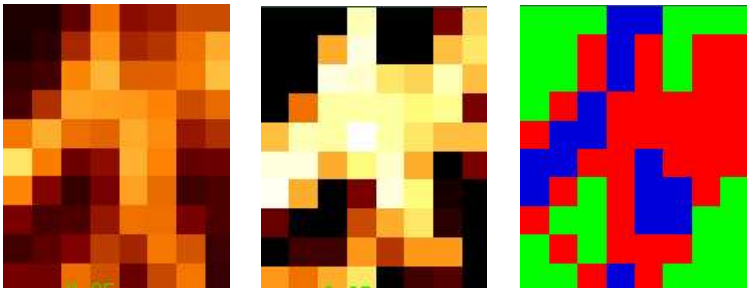

FA crop GA crop class crop

Figure 16: Transverse slice of a region of interest (ROI) from the genu of the corpus callosum. It is a similar ROI as in Tuch [41, fig. 12-f]. We show the fractional anisotropy map and the GA map computed from the HODT model. We attempt to threshold the GA measure to obtain the class map in the selected region. The green, blue and red color code represents isotropic, 1-fiber and multi-fiber diffusion respectively. As expected, we detect a multi-fiber area corresponding to the region of crossing in red.

7 Conclusion and Discussion

Overall, there are several contributions in this paper. Firstly, we proposed a new regularization algorithm to estimate a smoother ADC profile closer to the true ADC profile without noise. We chose a meaningful modified spherical harmonic basis to capture the physical constraints of the problem, defined a regularization term based on the smoothing properties of the Laplace-Beltrami operator for functions defined on the unit sphere and derived the linear transformation taking SH coefficients to HODT coefficients. We thus obtained a high order diffusion tensor. The method was tested against state of the art techniques from the literature on synthetic data, on a biological phantom and on real human brain data. Our experiments verify the equivalence of the diffusion tensor and the spherical harmonic formulations of the diffusivity profile up to a good numerical approximation. This is useful because it implies that any technique developed for the spherical harmonic formulation can be quickly and easily applied to the diffusion tensor formulation and vice versa.

Moreover, the continuous smoothing parameter λ generalizing the traditional least squares fitting algorithm for spherical harmonic series is appropriate whenever there is a sparsely sampled set of noisy data on a sphere and the expected approximation function is relatively smooth. However, minimizing the squared error is not the only important characteristic of a good approximation function. In particular, if we wish to be able to extract a fiber probability distribution for the voxel from our diffusivity profile model, we need the approximation to be sufficient to capture details up to the desired level of resolution. For example, over a data set that contained a large proportion of voxels with only a single fiber direction, an order-2 fit would certainly minimize the squared error from the actual data averaged over the entire data set. However, the higher order voxels would be modeled very poorly, making various tasks, such as tractography, considerably more difficult. For this reason, simple truncation, which is the equivalent to fitting the data with a lower order tensor, is not comparable to a procedure that retains higher-order detail, such as the proposed fit with a well-chosen regularization weight λ. Up to the resolution that we were considering, order-4 truncation was a valid choice of fitting procedure but has neither the general applicability nor the ability to retain detail at the 6^{th} and 8^{th} orders shown by the smoothness maximizing criterion we propose.

In addition to these contributions, another important part of the report is the careful study of the existing anisotropy measures for SH and HODT parametrization of the HARDI ADC profiles. We extended the study by attempting to classify the diffusion process from these anisotropy measures. This showed to be easier on synthetic data than on real data where selecting sensible thresholds is much harder. We have successfully reproduced the properties of the generalized anisotropy (GA) measure and clearly showed its advantages over the other scalar indices computed from spherical harmonics coefficients. In addition to being the high order generalization of the popular FA measure for DTI, it is stable and has the advantage of being scaled between 0 and 1. With a fast visual inspection, this allows the detection of non-Gaussian diffusion processes in cerebral regions from real data. This can potentially be of great help to clinicians and neurosurgeons.

Acknowledgments

The authors would like to thank the McConnel Brain Imaging Center (BIC) of McGill University and especially, J. Campbell, Kaleem Siddiqi, Peter Savadjiev, Vladimir V. Rymar and Bruce Pike for the rat cord dataset. This exchange was supported by the FFCR grant, the CRSNG Canada graduate scholarship and INRIA International internships program. Morever, thanks to S. Lehéricy and K. Ugurbil at the Center for Magnetic Resonance Research at the Minnesota University for the high angular human brain dataset. This part was partially supported by grants NSF-0404617 US-France (INRIA) Cooperative Research and the Région Provence-Alpes-Côte d'Azur. The authors would also like to thank Christophe Lenglet for his expertise and help on the subject and for his visualization softwares.

References

[1] D.C. Alexander. *An Introduction to Diffusion MRI: the Diffusion Tensor and Beyond. Chapter in "Visualization and Image Processing of Tensor Fields"*. Springer, 2005.

[2] D.C. Alexander, G.J. Barker, and S.R. Arridge. Detection and modeling of non-gaussian apparent diffusion coefficient profiles in human brain data. *Journal of Magnetic Resonance in Medicine*, 48:331–340, 2002.

[3] P.J. Basser, J. Mattiello, and D. LeBihan. Estimation of the effective self-diffusion tensor from the NMR spin echo. *Journal of Magnetic Resonance*, B(103):247–254, 1994.

[4] P.j. Basser, J. Mattiello, and D. LeBihan. MR diffusion tensor spectroscopy and imaging. *Biophysica*, (66):259–267, 1994.

[5] P.J. Basser and C. Pierpaoli. Microstructural and physiological features of tissues elucidated by quantitative diffusion tensor mri. *Journal of Magnetic Resonance*, 11:209–219, 1996.

[6] C.H. Brechbuhler, G. Gerig, and O. Kubler. Parametrization of closed surfaces for 3d shape description. *Computer Vision and Image Understanding*, 61:154–170, 1995.

[7] J. Campbell. *Diffusion Imaging of White Matter Fiber Tracts*. PhD thesis, McGill University, 2004.

[8] J. S. W. Campbell, K. Siddiqi, V. V. Rymar, A. F. Sadikot, and G. B. Pike. Flow-based fibre tracking with diffusion tensor and q-ball data: Validation and comparison to principal diffusion orientation techniques. *Neuroimage*, 2005, to appear.

[9] C. Chefd'hotel, D. Tschumperlé, R. Deriche, and O. Faugeras. Regularizing flows for constrained matrix-valued images. *Journal of Mathematical Imaging and Vision*, 20(1-2):147–162, 2004.

[10] Y. Chen, W. Guo, Q. Zeng, X. Yan, F. Huang, H. Zhang, G. He, B.C. Vemuri, and Y. Liu. Estimation, smoothing, and characterization of apparent diffusion coefficient profiles from high angular resolution dwi. In *Computer Vision and Pattern Recognition*, volume 1, pages 588–593, July 2004.

[11] Y. Chen, W. Guo, Q. Zeng, X. Yan, M. Rao, and Y. Liu. Apparent diffusion coefficient approximation and diffusion anisotropy characterization in dwi. In *Proceedings IPMI*, 2005, to appear.

[12] M. Descoteaux, E. Angelino, S. Fitzgibbons, and R. Deriche. Apparent diffusion coefficients from high angular resolution diffusion imaging: Estimations and applications. Technical report, INRIA Sophia Antipolis, Odysee Project Team, 2005, to appear.

[13] Q. Doug, R.C. Welsh, T.L. Chenevert, R.C. Carlos, P. Maly-Sundgren, D.M. Gomez-Hassan, and S.K. Mukherji. Clinical applications of diffusion tensor imaging. *Journal of Magnetic Resonance Imaging*, 19:6–18, 2004.

[14] Thomas Mareci Evren Ozarslan, Baba C. Vemuri. Fiber orientation mapping using generalized diffusion tensor imaging. In *ISBI*, 2004.

[15] L.R. Frank. Characterization of anisotropy in high angular resolution diffusion-weighted mri. *Magn. Res. Med*, 47:1083–1099, 2002.

[16] Quoc Thong Le Gia. *Approximation of linear partial differential equations on spheres*. PhD thesis, Texas A&M University, 2003.

[17] P.C. Hansen. The l-curve and its use in the numerical treatment of inverse problems. In P. Johnston, editor, *Computational Inverse Problems in Electrocardiology,*, pages 119–142, 2001.

[18] IEEE Computer Society. *Proceedings of the 9th International Conference on Computer Vision*, Nice, France, 2003. IEEE Computer Society Press.

[19] D. LeBihan, E. Breton, D. Lallemand, P. Grenier, E. Cabanis, and M. Laval-Jeantet. MR imaging of intravoxel incoherent motions: Application to diffusion and perfusion in neurologic disorders. *Radiology*, pages 401–407, 1986.

[20] C. Lenglet, R. Deriche, and O. Faugeras. Inferring white matter geometry from diffusion tensor MRI: Application to connectivity mapping. In T. Pajdla and J. Matas, editors, *Proceedings of the 8th European Conference on Computer Vision*, Prague, Czech Republic, May 2004. Springer–Verlag.

[21] C. Lenglet, M. Rousson, and R. Deriche. Segmentation of 3D probability density fields by surface evolution: Application to diffusion MRI. In *Proc. 7th Intl. Conf. on Medical Image Computing and Computer Assisted Intervention*, Saint-Malo, France, September 2004.

[22] C. Lenglet, M. Rousson, R. Deriche, and O. Faugeras. Toward segmentation of 3d probability density fields by surface evolution: Application to diffusion mri. Technical Report 5243, INRIA, June 2004.

[23] C. Lenglet, M. Rousson, R. Deriche, and O. Faugeras. Statistics on the manifold of multivariate normal distributions: Theory and application to diffsuion tensor mri. *Journal of Mathematical Imaging and Vision, Special Issue MIA'04*, 2005, in press.

[24] C. Lenglet, M. Rousson, R. Deriche, O. Faugeras, S. Lehéricy, and K. Ugurbil. A riemannian approach to diffusion tensor images segmentation. In *Proceedings IPMI*, 2005, to appear.

[25] Kalvis M.Jansons and Daniel C.Alexander. Persistent angular structure: new insights fom diffusion magnetic resonance imaging data. *Inverse Problems*, 19:1031–1046, 2003.

[26] M.E. Moseley, Y. Cohen, J. Mintorovitch, J. Kucharczyk, J. Tsuruda, P. Weinstein, and D. Norman. Evidence of anisotropic self-diffusion. *Radiology*, 176:439–445, 1990.

[27] P.A. Osment, K.J. Packer, M.J. Taylor, J. J. Attard, T. A. Carpenter, L. D. Hall, S. J. Doran, and N. J. Herrod. Nmr imaging of fluids in porous solids. *Phil. Trans. Roy. Soc.*, 333:441–452, 1990.

[28] E. Ozarslan and T. Mareci. Generalized diffusion tensor imaging and analytical relationships between diffusion tensor imaging and high angular resolution imaging. *Journal of Magnetic Resonance in Medicine*, 50:955–965, 2003.

[29] E. Ozarslan, B. Vemuri, and T. Mareci. Generalized scalar measures for diffusion mri using trace, variance and entropy. *Journal of Magnetic Resonance in Medicine*, 53:866–876, 2005.

[30] C. Poupon. *Détection des faisceaux de fibres de la substance blanche pour l'étude de la connectivité anatomique cérébrale.* PhD thesis, Ecole Nationale Supérieure des Télécommunications, December 1999.

[31] M. Rao, Y. Chen, B.C. Vemuri, and F. Wang. Cumulative residual entropy: A new measure of information. *IEEE Transactions on Information Theory*, 50:1220–1228, 2004.

[32] J. Sijbers, A. J. den Dekker, J. Van Audekerke, M. Verhoye, and D. Van Dyck. Estimation of the noise in magnitude mr images. *Magnetic Resonance Imaging*, 16(1):87–90, 1998.

[33] Jan Sijbers. *Signal and Noise Estimation from Magnetic Resonance Images*. PhD thesis, Universiteit Antwerpen, 1998.

[34] N. Sochen, R. Deriche, and L. Lopez-Perez. The beltrami flow over implicit manifolds. In *Proceedings of the 9th International Conference on Computer Vision* [18].

[35] N. Sochen, R. Deriche, and L. Lopez-Perez. Variational beltrami flows over manifolds. In *International Conference on Image Processing*, 2003.

[36] Olle Soderman and Bengt Jonsson. Restricted diffusion in cylindrical geometry. *Journal Of Magnetic Resonance*, 1995.

[37] E.O. Stejskal and J.E. Tanner. Spin diffusion measurements: spin echoes in the presence of a time-dependent field gradient. *Journal of Chemical Physics*, 42:288–292, 1965.

[38] D. Tschumperlé and R. Deriche. Diffusion tensor regularization with constraints preservation. In *IEEE Computer Society Conference on Computer Vision and Pattern Recognition*, Kauai Marriott, Hawaii, December 2001.

[39] D. Tschumperlé and R. Deriche. Variational frameworks for DT-MRI estimation, regularization and visualization. In *Proceedings of the 9th International Conference on Computer Vision* [18].

[40] D. Tuch. *Diffusion MRI of Complex Tissue Structure*. PhD thesis, Harvard University and Massachusetts Institute of Technology, 2002.

[41] D. Tuch. Q-ball imaging. *Journal of Magnetic Resonance in Medicine*, 52:1358–1372, 2004.

[42] D.S. Tuch, J.W. Belliveau, T.G. Reese, and V.J. Wedeen. High angular resolution imaging of the human brain. In *Proceedings of the International Society for the Magnetic Resonance in Medecine*, Philadelphia, April 1999.

[43] D.S. Tuch, T.G. Reese, M.R. Wiegell, N.G. Makris, J.W. Belliveau, and V.J. Wedeen. High angular resolution diffusion imaging reveals intravoxel white matter fiber heterogeneity. *Magn. Res. Med.*, 48:577–582, 2002.

[44] E. von dem Hagen and M. Henkelman. Orientational diffusion reflects fiber structure within a voxel. *Journal of Magnetic Resonance in Medicine*, 48:454–459, 2002.

[45] Z. Wang, B.C. Vemuri, Y. Chen, and T. Mareci. Simultaneous smoothing and estimation of the tensor field from diffusion tensor mri. In *IEEE Conference on Computer Vision and Pattern Recognition*, volume I, pages 461–466, Madison, Wisconsin (United States), June 2003.

[46] V.J. Wedeen, T. G. Reese, D.S. Tuch, J.-G. Dou, R.M. Weiskoff, and D. Chessler. Mapping fiber orientation spectra in cerebral white matter with fourier-transform diffusion mri. In *Proceedings of the International Society for the Magnetic Resonance in Medecine*, page 321, 1999.

[47] C.F Westin, S.E Maier, H. Mamata, A. Nabavi, F.A. Jolesz, and R. Kikinis. Processing and visualization for diffusion tensor MRI. In *In proceedings of Medical Image Analysis*, volume 6(2), pages 93–108, 2002.

A Relation of Spherical Harmonics to the HODT

Here, we aim to prove that the M matrix (Eq. 38) is simply a change of basis, i.e. that for all integers $n \geq 0$, the diffusion tensor polynomials of rank $2n$ and the modified set of spherical harmonics up through rank $2n$ both form a basis for the same space of functions. We note that this implies that M is invertible. Before proving this, we will make some preliminary comments. Firstly, the spherical harmonics of order ℓ are defined to be the restrictions of homogeneous harmonic polynomials of order ℓ to the unit sphere [16]. Both the standard set of spherical harmonics and the modified set we introduce in this paper are just particular choices of basis for this space. Secondly, the diffusion tensor polynomials of rank ℓ are simply the set of unique monomials of degree ℓ, i.e. $\{x^a y^b z^c | a, b, c \geq 0, a+b+c = \ell\}$ which we also restrict to the unit sphere. Finally, both of the above sets (modified spherical harmonics of order $\leq 2n$ and diffusion tensor polynomials of rank $2n$) are linearly independent and have the same number of elements. Therefore, it suffices to show that all the elements in one set can be expressed as linear combinations of elements in the other set to prove that both sets form a basis for the same space.

Theorem: For all integers $n \geq 0$, the diffusion tensor polynomials of rank $2n$, i.e. $\{x^a y^b z^c | a, b, c \geq 0, a+b+c = \ell\}$, restricted to the sphere, and the set of modified spherical harmonics of order $\leq 2n$ form a basis for the same space of functions.

Proof: Our approach will be to show that every even order homogeneous harmonic polynomial restricted to the unit sphere of order $\leq 2n$ can be expressed as a linear combination of the diffusion tensor polynomials of rank $2n$. As discussed above, this result is equivalent to the statement of the theorem. We proceed by induction. Note that we will use $\sim$ to denote "is proportional to".

Base case: For $n = 0$, the set of homogeneous harmonic polynomials of order 0 restricted to the unit sphere is simply the set of constant functions, and we have that

$$\{x^a y^b z^c | a, b, c >= 0, a+b+c = 0\} = x^0 y^0 z^0 \sim 1.$$

Therefore, any homogeneous harmonic polynomial of order 0 restricted to the unit sphere is simply a linear scaling of the unique diffusion tensor polynomial of order 0.

Inductive step: Assume that all homogeneous harmonic polynomials of order $\leq 2n-2$ can be expressed as linear combinations of diffusion tensor polynomials of rank $2n-2$. Since we are restricted to the sphere, we can multiply each of these formulas by $x^2+y^2+z^2 = 1$ to express each of the homogeneous harmonic polynomials of order $\leq 2n-2$ as linear combinations of diffusion tensor polynomials of rank $2n$. For example, the homogeneous harmonic polynomial of order 2, xz, is itself a diffusion tensor polynomial of rank 2. However, it can also be written as a linear combination of rank 4 diffusion tensor polynomials in the following way: $xz(x^2+y^2+z^2) = x^3z + xy^2z + xz^3$. Furthermore, every homogeneous harmonic polynomial of order $2n$ can be expressed as a linear combination of diffusion tensor polynomials of rank $2n$ simply because the set of unique monomials of degree $2n$ spans the set of polynomials of degree $2n$. This completes the proof.

We now proceed to give a brief example. Below we express each of the elements of our modified SH basis of order ≤ 2 (Fig. 4) in terms of linear combinations of diffusion tensor polynomials of rank 2. (Restricting to the unit sphere gives, as in standard spherical coordinates, the relations: $x = \cos\phi \sin\theta$, $y = \sin\phi \sin\theta$, $z = \cos\theta$ and $1 = x^2 + y^2 + z^2$).

$$
\begin{array}{lll}
Y_1 & \sim 1 & \sim x^2 + y^2 + z^2 \\
Y_2 & \sim \sin^2\theta \cos(2\phi) & \\
 & \sim \sin^2\theta(\cos^2\phi - \sin^2\phi) & \sim x^2 - y^2 \\
Y_3 & \sim \sin\theta \cos\theta \cos\phi & \sim xz \\
Y_4 & \sim 3\cos^2\theta - 1 & \\
 & \sim 3z^2 - (x^2 + y^2 + z^2) & \sim 2z^2 - x^2 - y^2 \\
Y_5 & \sim \sin\theta \cos\theta \sin\phi & \sim yz \\
Y_6 & \sim \sin^2\theta \sin(2\phi) & \\
 & \sim \sin^2\theta(2\sin\phi\cos\phi) & \sim xy
\end{array}
$$

With linear combination of the Y_1, Y_2 and Y_4 terms, one can obtain the monomials x^2, y^2 and z^2. Hence, the modified basis of order 2 spans the set of degree two monomials.

This result explains why fitting with the diffusion tensor formulation and fitting with the spherical harmonic formulation are equivalent as seen in, for example, the similarity of the $\lambda = 0$ fit and the linear regression HODT fit in Table 2 and Table 3.

Unité de recherche INRIA Sophia Antipolis
2004, route des Lucioles - BP 93 - 06902 Sophia Antipolis Cedex (France)

Unité de recherche INRIA Futurs : Parc Club Orsay Université - ZAC des Vignes
4, rue Jacques Monod - 91893 ORSAY Cedex (France)
Unité de recherche INRIA Lorraine : LORIA, Technopôle de Nancy-Brabois - Campus scientifi que
615, rue du Jardin Botanique - BP 101 - 54602 Villers-lès-Nancy Cedex (France)
Unité de recherche INRIA Rennes : IRISA, Campus universitaire de Beaulieu - 35042 Rennes Cedex (France)
Unité de recherche INRIA Rhône-Alpes : 655, avenue de l'Europe - 38334 Montbonnot Saint-Ismier (France)
Unité de recherche INRIA Rocquencourt : Domaine de Voluceau - Rocquencourt - BP 105 - 78153 Le Chesnay Cedex (France)

Éditeur
INRIA - Domaine de Voluceau - Rocquencourt, BP 105 - 78153 Le Chesnay Cedex (France)
http://www.inria.fr
ISSN 0249-6399